Connecting the Local Response to Abyssal Mixing to the Basin-Scale Circulation

HENRY G. PETERSON[a] AND JÖRN CALLIES[a]

[a] *California Institute of Technology, Pasadena, California*

(Manuscript received 9 July 2025, in final form 13 November 2025, accepted 10 December 2025)

ABSTRACT: The circulation of the abyssal ocean is thought to be sustained by turbulence over a rough seafloor. Over sloping topography, this bottom-enhanced mixing produces diapycnal upwelling within a thin bottom boundary layer and downwelling aloft. Simplified theories have been developed to understand this local response to mixing, for example, by assuming an along-slope symmetry and imposing a constraint on the cross-slope transport. Ultimately, the local response to mixing on slopes must be connected to the basin-scale circulation; however, the barotropic transport must conserve potential vorticity. This coupling between the local response to mixing and the basin-scale circulation is studied here in the context of an idealized bowl-shaped basin using boundary layer theory and numerical solutions of the planetary geostrophic equations. In the absence of wind forcing and the joint effect of baroclinicity and relief (JEBAR), the leading-order barotropic transport is directed along f/H contours, where f is the planetary vorticity and H is the depth. The local response to mixing is coupled to this barotropic circulation. It can be thought of as simultaneously constrained by the barotropic circulation and forcing it via a bottom stress curl. If f/H contours are closed, a strong barotropic circulation spins up along them as in simplified theories of the local response in the absence of along-slope variations. If these contours intersect the boundary, a case more typical in the real ocean, the barotropic transport is suppressed. This decouples the leading-order local response from the large-scale circulation and intensifies bottom boundary layer upwelling.

KEYWORDS: Abyssal circulation; Mixing; Boundary layer

1. Introduction

After dense Antarctic Bottom Water fills the global abyssal ocean basins (e.g., Lumpkin and Speer 2007; Talley 2013), it must undergo diapycnal transformation to return to the surface and close the overturning (e.g., Munk 1966; Munk and Wunsch 1998; Ferrari 2014). This transformation is achieved by small-scale turbulent mixing, which we now understand to be bottom-enhanced over rough topography (e.g., Polzin et al. 1997; Ledwell et al. 2000; Waterhouse et al. 2014), where internal waves are prone to breaking (e.g., Garrett and Kunze 2007; Nikurashin and Ferrari 2011). Considering the one-dimensional balance between diapycnal advection and diffusion in the vertical, bottom-enhanced mixing must confine the upwelling needed to close the overturning to the bottom few meters of the water column (e.g., Ferrari et al. 2016; de Lavergne et al. 2016; McDougall and Ferrari 2017). Recent observations from a canyon in the Rockall Trough are consistent with this prediction (Wynne-Cattanach et al. 2024). How this bottom-enhanced mixing on slopes shapes the hydrography and basin-scale circulation, however, remains poorly understood.

In some circumstances, it is possible to fully describe the local response of a water column to bottom-enhanced mixing using a one-dimensional model. Canonically, this model of a rotating and stratified fluid over a sloping seafloor assumes no cross- or along-slope variations of the flow, pressure, and buoyancy anomalies (e.g., Phillips 1970; Wunsch 1970; Thorpe 1987; Garrett et al. 1993). It produces a peculiar steady-state solution, however, in which the vertically integrated cross-slope transport is set by the local slope and interior mixing strength, and it approaches this steady state diffusively over thousands of years for typical abyssal parameters (MacCready and Rhines 1991; Thompson and Johnson 1996). The inference that the local response dictates the net transport of the global circulation fails to consider that the coupling goes both ways. In Peterson and Callies (2022, hereafter PC22), we took a step toward accounting for the large-scale context in the local response to mixing. In the absence of along-slope variations, the vertically integrated cross-slope transport should vanish to satisfy volume conservation. The effects of this constraint are illustrated in Fig. 1 for a buoyancy field generated by bottom-enhanced mixing of fluid with initially constant stratification over a uniform slope (Fig. 1a; see section 2 for details). The requirement that all the upwelling in the bottom boundary layer (BL) be returned in the interior above sets up a secondary cross-slope circulation (Fig. 1b). To allow for a transport constraint, the one-dimensional model must be modified to include a cross-slope barotropic pressure gradient $\partial_x P$. As the cross-slope flow returns in the interior, it is turned in the along-slope direction by the Coriolis acceleration and put in geostrophic balance with the cross-slope pressure gradient (Fig. 1c). The interior along-slope flow is then enabled to spin up rapidly, rather than being controlled by diffusion. This transport-constrained model fully describes the spinup of mixing-generated flow in the absence of along-slope variations, capturing the flow spun-up by bottom-enhanced mixing over an idealized ridge, for example (Ruan and Callies 2020).

The PC22 model relies on symmetry in the along-slope direction to provide enough constraints to solve for the local response. This symmetry is broken if, for instance, meridional variations in the planetary vorticity f are allowed. In general, the local response is coupled to the basin-scale barotropic

Corresponding author: Henry Peterson, hgpeterson@caltech.edu

DOI: 10.1175/JPO-D-25-0159.1

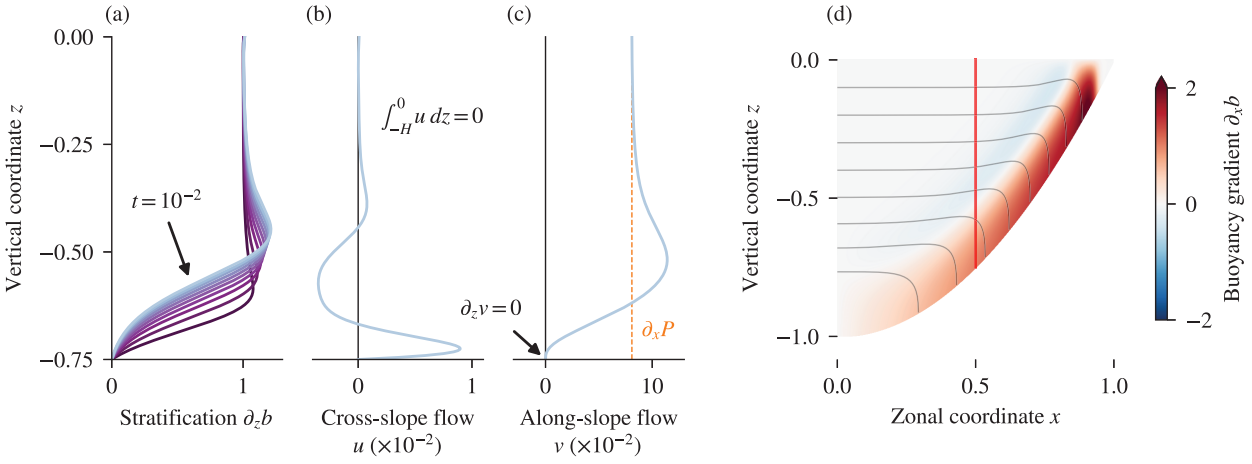

FIG. 1. Illustration of buoyancy field generated from bottom-enhanced diffusion in the vertical and resulting flow predicted from the uniform slope model of PC22. For details of the dynamical equations and nondimensionalization, refer to section 2. (a) Vertical profiles of stratification $\partial_z b$ at a column depth of $H = 0.75$ corresponding to the red line in (d), with time ranging from $t = 10^{-3}$ (purple) to $t = 10^{-2}$ (light blue) at a spacing of 10^{-3}. For the remainder of the paper, we freeze the buoyancy field at $t = 10^{-2}$. (b) Cross-slope flow u and (c) along-slope flow v inferred from the uniform slope model at $t = 10^{-2}$. Parameters are as in section 3: an Ekman number of $\varepsilon = 2 \times 10^{-2}$, turbulent viscosity of $\nu = 1$, and nondimensional slope $\theta = \pi/4$ corresponding to the slope at the red line in (d). (d) Isopycnals (gray lines) and horizontal buoyancy gradient $\partial_x b$ (colors) at $t = 10^{-2}$ in a bowl geometry $H = 1 - x^2 - y^2$ for $0 \le x \le 1$ and $y = 0$.

circulation. The net transport of the local response is constrained by the barotropic circulation, as in PC22 (though now in both directions). At the same time, the curl of the bottom stress due to the local response is itself a forcing in the barotropic problem. Classical models of the barotropic circulation (e.g., Stommel 1948; Munk 1950; Robinson 1970; Rattray 1982; Mertz and Wright 1992) use a simple form of the bottom stress without considering buoyancy effects. In this work, we use standard Ekman BL theory (e.g., Pedlosky 1979; Vallis 2017) to derive explicit expressions for the bottom stress in terms of the barotropic transport, buoyancy field, and wind stress. This allows us to leverage intuition from textbook barotropic dynamics (e.g., Pedlosky 1979; Vallis 2017) to understand the connection between the local response to mixing and the basin-scale circulation.

To understand this coupling in a simple context, we study the flow produced by a prescribed buoyancy field, neglecting buoyancy advection. In particular, for a buoyancy field dependent only on the depth of the fluid H (as in the purely mixing-generated field in Fig. 1), the joint effect of baroclinicity and relief (JEBAR) drops out of the barotropic vorticity equation. Furthermore, we find that the bottom stress curl from Ekman BL theory is not a leading-order term in the barotropic vorticity budget in the interior of the basin. In the absence of a wind stress curl, therefore, the leading-order barotropic flow in this case must follow f/H contours. These contours tend to be open and fairly longitudinal in the real ocean, but they can close around large enough topographic features (e.g., Dewar 1998, cf. Fig. 2). These two different topological states of the f/H contours in an abyssal basin strongly alter the qualitative barotropic dynamics. Flow along closed contours is unencumbered in the inviscid equations of motion, allowing for a strong barotropic response (e.g., Kawase 1993; Thompson 1995; Hallberg and Rhines 1996). Open contours, on the other hand, intersect the boundary on the equator or at vertical sidewalls, thereby destroying the leading-order barotropic circulation. The first case only slightly modifies the circulation compared to the local response derived from the PC22 model, with the barotropic flow now directed along f/H contours rather than simply along slope. These are one and the same on an f plane, implying that the PC22 model would still apply (provided that the assumption of along-slope symmetry is still a good one). The second case, however, would require a modification of the local theory to include a constraint on both the cross- and along-slope transports, as we will see below.

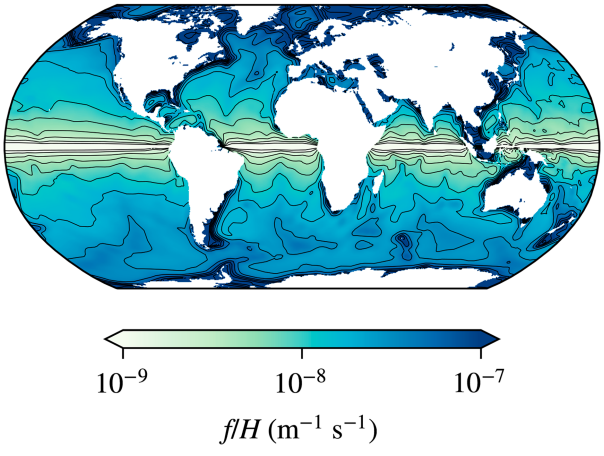

FIG. 2. Contours of f/H for the global ocean using bathymetry data from Smith and Sandwell (1997, updated). The data are smoothed by averaging over a 500-km-diameter circle at each point. Contours that appear to intersect the boundary are actually directed along coastlines before converging at the equator.

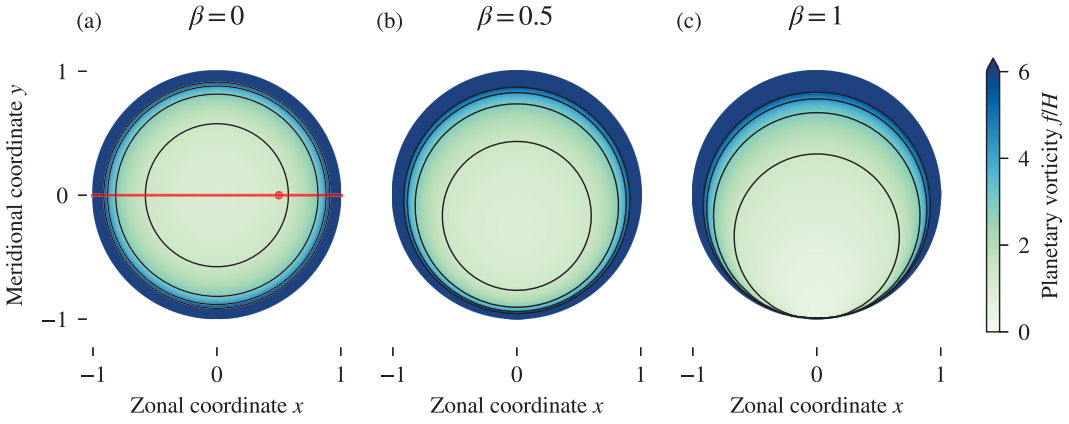

FIG. 3. Contours of f/H in a circular midlatitude basin for $H = 1 - x^2 - y^2$ and (a) $f = 1$, (b) $f = 1 + 0.5y$, and (c) $f = 1 + y$. The red line and circle in (a) indicate where the zonal slices in Fig. 4 and the profiles in Fig. 5 are taken, respectively.

In section 2, we begin by introducing the planetary geostrophic (PG) formulation and an idealized abyssal basin that will serve as our testbed for the remainder of the paper. We then dive into the phenomenology of numerical solutions for the PG circulation within this basin in section 3. The hydrography is set by bottom-enhanced diffusion of buoyancy starting from flat isopycnals, and the resulting flow is computed on an f plane and two β planes, one with closed f/H contours and one with open ones. In section 4, we use intuition from these numerically derived circulations to motivate a theoretical description of the connection between the local baroclinic response to mixing and the barotropic circulation. A discussion of the significance of these results and key conclusions are provided in sections 5 and 6, respectively.

2. A model problem for an abyssal basin

The goal of this study is to understand how the local response to bottom-enhanced mixing interacts with the basin-scale circulation. With this in mind, we consider an idealized, closed basin to isolate this physics. We choose a bowl-shaped domain defined by a parabolic depth function, which, in the nondimensional coordinates defined below, sets a coastline along the unit circle centered at the origin in the x–y plane (Fig. 3). The symmetry about the origin is the main reason for using this geometry as opposed to a rectangular basin more often employed in idealized studies of the large-scale circulation (e.g., Ito and Marshall 2008; Wolfe and Cessi 2011; Nikurashin and Vallis 2011; Callies and Ferrari 2018; Jansen and Nadeau 2019). By varying β in $f(y) = f_0 + \beta y$, we can examine the dynamics under different f/H contour configurations, with $f/H = (1 + \beta y)/(1 - x^2 - y^2)$ under the nondimensionalization defined below. On an f plane ($\beta = 0$), this yields axisymmetric f/H contours (Fig. 3a), vastly simplifying the description of the coupling between the local and global dynamics, as we will see in the next section. As β is increased, the f/H contours shift southward (Figs. 3b,c), breaking this symmetry and demanding a more general treatment of the problem. Once $\beta \geq 1$, the domain includes the equator, allowing these contours to open,[1] perhaps more representative of most of the real ocean's f/H contours (Fig. 2). As anticipated in the introduction and explained in detail in the next section, the basin-scale dynamics are qualitatively different for open versus closed contours. In this way, the three cases considered here ($\beta = 0, 0.5, 1$) cover three key scenarios, allowing us to develop and test a general theory for the connection between the local response to mixing and the basinwide abyssal circulation.

a. Planetary geostrophic equations

To put the focus on the mixing-generated abyssal circulation, we employ the PG approximation (e.g., Pedlosky 1979; Vallis 2017). The PG scaling assumes large horizontal scales and small Rossby numbers, removing the inertial terms in the momentum equations. This filters out fast-time-scale dynamics such as small-scale turbulence, internal waves, and baroclinic eddies, but we interpret the PG flow as the residual flow after a thickness-weighted average over these transients, with their effects included as parameterized Eliassen–Palm and diapycnal fluxes (e.g., Young 2012). As described in the next section, however, we do not consider the effects of an eddy parameterization in this work. The dimensional PG equations in Cartesian space (x, y, z) are

$$-fv = -\frac{\partial p}{\partial x} + \frac{\partial}{\partial z}\left(\nu \frac{\partial u}{\partial z}\right), \tag{1}$$

$$fu = -\frac{\partial p}{\partial y} + \frac{\partial}{\partial z}\left(\nu \frac{\partial v}{\partial z}\right), \tag{2}$$

[1] While, topologically, the contours still form closed loops, they are "open" in the sense that they touch the boundary, where $H = 0$, such that a frictionless barotropic along-contour circulation cannot be sustained.

$$\frac{\partial p}{\partial z} = b, \tag{3}$$

$$\nabla \cdot \mathbf{u} = 0, \tag{4}$$

$$\frac{\partial b}{\partial t} + \mathbf{u} \cdot \nabla b = \frac{\partial}{\partial z}\left(\kappa \frac{\partial b}{\partial z}\right), \tag{5}$$

where $\mathbf{u} = (u, v, w)$ is the velocity vector, b is the buoyancy, and ν and κ are the turbulent viscosity and diffusivity, respectively. We apply no-slip ($\mathbf{u} = 0$) and no-flux ($\partial_z b = 0$) boundary conditions at the bottom that is located at $z = -H(x, y)$. At the surface ($z = 0$), we demand no normal flow ($w = 0$) with a wind stress forcing ($\nu \partial_z \mathbf{u}_\perp = \tau$) and a fixed uniform buoyancy ($b = 0$). In this formulation, we neglect horizontal diffusion terms in the horizontal momentum equations [(1) and (2)]. For small-scale isotropic turbulence, this is consistent with the assumption of a small aspect ratio. If the diffusion terms are instead interpreted as parameterizing Eliassen–Palm fluxes, then this assumption amounts to neglecting momentum fluxes, which is conventionally thought to be justified (e.g., Gent and Mcwilliams 1990). These terms, as well as diffusion in the hydrostatic equation [(3)], are, however, present in the simulations for numerical stability (see section 3 and appendix A).

These PG dynamics can be viewed separately as an evolution equation for buoyancy [(5)] and an inversion statement for the flow [(1)–(4)]. For this study, we aim to understand the inversion statement in isolation, leaving an analysis of the full PG system for future work. To consider a flow field in the context of abyssal mixing, we apply the inversion statement to a buoyancy field generated by pure bottom-enhanced diffusion. We solve

$$\frac{\partial b}{\partial t} = \frac{\partial}{\partial z}\left(\kappa \frac{\partial b}{\partial z}\right) \tag{6}$$

with an initial condition of flat isopycnals, $b_0 = N^2 z$, where N^2 is the initial stratification. This setting is, of course, a major simplification of the dynamics; in reality, the ocean is thought to be in a nearly steady state, with advection in balance with diffusion: $\mathbf{u} \cdot \nabla b = \partial_z(\kappa \partial_z b)$ (Munk 1966). Instead, the buoyancy field satisfying (6) simply mixes toward $b = 0$, and the flow derived from the inversion statement has no impact on this evolution. As we will see in the following sections, however, the phenomenology of the PG inversion alone is rich enough to warrant isolated study, and its understanding can be used as a stepping stone for studying the complete dynamics.

b. Nondimensionalization and parameters

To isolate key parameters in the problem, we work with the nondimensional PG equations for the remainder of the paper. We define the characteristic scales for the horizontal and vertical coordinates, velocities, Coriolis parameter, and mixing coefficients such that

$$x, y \sim L, \quad z \sim H_0, \quad u, v \sim U_0,$$
$$w \sim \frac{U_0 H_0}{L}, \quad f \sim f_0, \quad \nu \sim \nu_0, \quad \kappa \sim \kappa_0. \tag{7}$$

Unlike in quasigeostrophic theory, the PG equations do not impose an explicit background stratification. For the simple diffusion problem considered in (6), however, the initial condition sets a natural scaling for buoyancy, $b \sim N^2 H_0$. Finally, we assume that the horizontal pressure gradient terms in (1) and (2) scale with the Coriolis terms, that the buoyancy also scales with the pressure scale divided by H_0 from hydrostatic balance in (3), and that time scales advectively:

$$p \sim f_0 U_0 L, \quad b \sim \frac{f_0 U_0 L}{H_0} = N^2 H_0, \quad t \sim \frac{L}{U_0}. \tag{8}$$

Applying these scales to (1)–(5) yields the following nondimensional PG equations:

$$-\tilde{f}\tilde{v} = -\frac{\partial \tilde{p}}{\partial \tilde{x}} + \varepsilon^2 \frac{\partial}{\partial \tilde{z}}\left(\tilde{\nu} \frac{\partial \tilde{u}}{\partial \tilde{z}}\right), \tag{9}$$

$$\tilde{f}\tilde{u} = -\frac{\partial \tilde{p}}{\partial \tilde{y}} + \varepsilon^2 \frac{\partial}{\partial \tilde{z}}\left(\tilde{\nu} \frac{\partial}{\partial \tilde{z}}\right), \tag{10}$$

$$\frac{\partial \tilde{p}}{\partial \tilde{z}} = \tilde{b}, \tag{11}$$

$$\tilde{\nabla} \cdot \tilde{\mathbf{u}} = 0, \tag{12}$$

$$\mu\rho\left(\frac{\partial \tilde{b}}{\partial \tilde{t}} + \tilde{\mathbf{u}} \cdot \tilde{\nabla}\tilde{b}\right) = \varepsilon^2 \frac{\partial}{\partial \tilde{z}}\left(\tilde{\kappa} \frac{\partial \tilde{b}}{\partial \tilde{z}}\right), \tag{13}$$

where $\varepsilon^2 = \nu_0/(f_0 H_0^2)$ is the Ekman number, $\rho = N^2 H_0^2/f_0^2 L^2$ is the Burger number, and $\mu = \nu_0/\kappa_0$ is the turbulent Prandtl number. The wind stress boundary condition at $\tilde{z} = 0$ is now $\varepsilon^2 \tilde{\nu} \partial_{\tilde{z}} \tilde{\mathbf{u}}_\perp = \tilde{\boldsymbol{\tau}}$. We will work with nondimensional variables for the remainder of the paper, dropping the $\tilde{}$ decoration for visual clarity.

Typical order-of-magnitude scales for an abyssal basin are

$$f_0 \approx 10^{-4}\,\mathrm{s}^{-1}, \quad H_0 \approx 10^3\,\mathrm{m}, \quad N \approx 10^{-3}\,\mathrm{s}^{-1}, \quad L \approx 10^6\,\mathrm{m}, \tag{14}$$

yielding a Burger number of $\varrho \approx 10^{-4}$. Over rough topography, observations show enhanced turbulence associated with a turbulent diffusivity on the order of $\kappa_0 \approx 10^{-3}\ \mathrm{m^2\ s^{-1}}$ in an abyssal mixing layer roughly a few hundred meters above the bottom (e.g., Waterhouse et al. 2014). Although the magnitude of the turbulent viscosity is less clear, it is reasonable to assume that, for weakly stratified abyssal waters, small-scale mixing of buoyancy would occur on similar scales to the mixing of momentum, implying that $\nu_0 \sim \kappa_0$, or $\mu \sim 1$ (e.g., Caulfield 2021). Parameterizing the Eliassen–Palm flux of submesoscale baroclinic eddies generated in abyssal mixing layers would require $\mu \gg 1$ (e.g., Wenegrat et al. 2018; Callies 2018), but we reserve a complete study of how eddy restratification affects the basin-scale circulation for future work. Taking $\nu_0 = \kappa_0 = 10^{-3}\ \mathrm{m^2\ s^{-1}}$ then puts ε at about 3×10^{-3}. To properly resolve the BL in the numerical model described in the next section, we instead choose a magnified value of $\varepsilon = 2 \times 10^{-2}$, which thickens the BL and speeds up diffusion but does not qualitatively change the solutions.

For scales relevant to the basin-scale abyssal circulation, we therefore make the following assumptions:

$$\varepsilon \ll 1 \quad \text{and} \quad \mu\varrho \sim \varepsilon^2. \tag{15}$$

The first of these assumptions motivates the use of BL theory (section 4), as a typical ratio of the bottom Ekman layer thickness $\delta = \sqrt{2\nu_0/f_0}$ to the column depth H_0 is $\sqrt{2}\,\varepsilon \approx 2.8 \times 10^{-2}$ (this translates to a dimensional BL thickness of 28 m given $H_0 = 1$ km). According to the BL theory derived in Peterson and Callies (2023, hereafter PC23), the cross-slope flow in the PC22 model is of $O(\varepsilon)$ in the BL and $O(\varepsilon^2)$ in the interior. Along with the second scaling assumption in (15), this would suggest that, in the absence of along-slope variations, advection of buoyancy in (13) is of higher order in ε than diffusion. While this may no longer be the case once along-slope variations are allowed, as we will show below, it further motivates our simplification of the buoyancy equation to pure diffusion [(6)] as a first look at the basin-scale dynamics. We therefore solve the nondimensional buoyancy diffusion equation in the vertical,

$$\mu\varrho\frac{\partial b}{\partial t} = \varepsilon^2\frac{\partial}{\partial z}\left(\kappa\frac{\partial b}{\partial z}\right), \tag{16}$$

with the initial condition $b = z$ and boundary conditions $\partial_z b = 0$ at $z = -H$ and $b = 0$ at $z = 0$.

3. Numerical inversions for the three-dimensional mixing-driven flow

Before developing a mathematical theory, in this section, we build intuition for the phenomenology of the mixing-generated circulation from numerical solutions of the idealized problem described above. We use the finite element method to integrate the diffusion equation [(16)] forward in time and solve a form of the PG inversion [(9)–(12)] with an artificially large aspect ratio for numerical stability (see appendix A). As expected, on an f plane, the circulation in the bowl is axisymmetric, allowing us to describe the local dynamics using the theory from PC22 and PC23. The tilted isopycnals due to mixing rapidly spin up a far-field flow that circumnavigates the basin. On a β plane, the barotropic circulation shifts southward following f/H contours. For open contours, the barotropic transport is nearly zero throughout the domain, constraining the vertical structure of the flow and leading to stronger BL transport.

a. Numerical approach

Despite the simplified form of the PG inversion [(9)–(12)] compared to the full Boussinesq system, solving the problem numerically in an arbitrary domain and with high resolution in the bottom BL can still prove challenging. The geometrically flexible finite element method is a natural choice for this problem, but the small aspect ratio of the ocean destabilizes standard techniques (e.g., Guillén-González and Rodríguez-Galván 2015). To leverage the robustness of standard finite element techniques without altering the qualitative behavior of the circulation, we artificially increase the aspect ratio $\alpha = H_0/L$ to 1/2, reintroducing both diffusion in the vertical momentum equation and horizontal diffusion of momentum. This "aspect ratio trick" has been utilized in a number of other models (e.g., Kuang et al. 2005; Garner et al. 2007; Salmon 2009). We consider the effects of the approximation in appendix A.

With horizontal diffusion terms included, the PG inversion is equivalent to rotating Stokes flow, which may be solved efficiently and accurately using textbook mixed finite element methods (e.g., Hughes 1987; Elman et al. 2014). We use P_2–P_1 elements (sometimes also called Taylor–Hood elements), where velocity and pressure are represented by quadratic and linear basis functions, respectively. For this method, the energy-normed error scales quadratically with mesh resolution. To resolve the BL scale, we discretize the domain using an unstructured tetrahedral mesh with a uniform resolution of 10^{-2} generated using Gmsh (Geuzaine and Remacle 2009). We use the generalized minimum residual method (GMRES) to iteratively solve the resulting linear system for velocity and pressure given the buoyancy field. For simplicity, we do not specify a spatial structure in the nondimensional turbulent viscosity, setting $\nu = 1$ everywhere. The implementation in Julia (Bezanson et al. 2017), which makes use of Gridap.jl for finite elements (Badia and Verdugo 2020), Krylov.jl for iterative solvers (Montoison and Orban 2023), and CUDA.jl for graphics processing unit (GPU) support (Besard et al. 2019), is hosted on GitHub (https://github.com/hgpeterson/nuPGCM).

As stated previously, we apply the PG inversion to a buoyancy field generated by bottom-enhanced diffusive mixing in the vertical [see (16)]. We choose a nondimensional turbulent diffusivity profile that decays exponentially with height above bottom,

$$\kappa(x, y, z) = 10^{-2} + \exp\left[-\frac{z + H(x, y)}{0.1}\right], \tag{17}$$

qualitatively consistent with observations over rough topography on the Mid-Atlantic Ridge (e.g., Polzin et al. 1997; Callies 2018). Equation (16) is then discretized using P_2 finite elements for buoyancy and integrated in time using the second-order semi-implicit Crank–Nicolson method. Starting from flat isopycnals $b = z$, a bottom mixing layer with $\partial_z b < 1$ instantaneously develops to satisfy the no-flux boundary condition (Fig. 1a). This mixing layer grows diffusively—first rapidly near the bottom, where $\kappa \sim O(1)$, then more slowly once it reaches the interior, where $\kappa \sim O(10^{-2})$—eroding the stratification in the column toward zero. When applied along the sloping bowl bathymetry, this vertical mixing bends isopycnals into the slopes, generating cross-slope buoyancy gradients (Fig. 1d). These buoyancy gradients, as we will see in the following sections, spin up a basin-scale circulation described by the PG inversion. In the remainder of the paper, we analyze the PG inversion for the buoyancy field at $t = 10^{-2}$ (light-blue line in Fig. 1a). Using the scales defined above, this corresponds to a dimensional time of about $t^* = t/f_0\varrho \approx 10$ days. This short time reflects the artificially enhanced Ekman number, which accelerates the rate of diffusion by a factor of ~100. We now explore the phenomenology of the circulation set up by

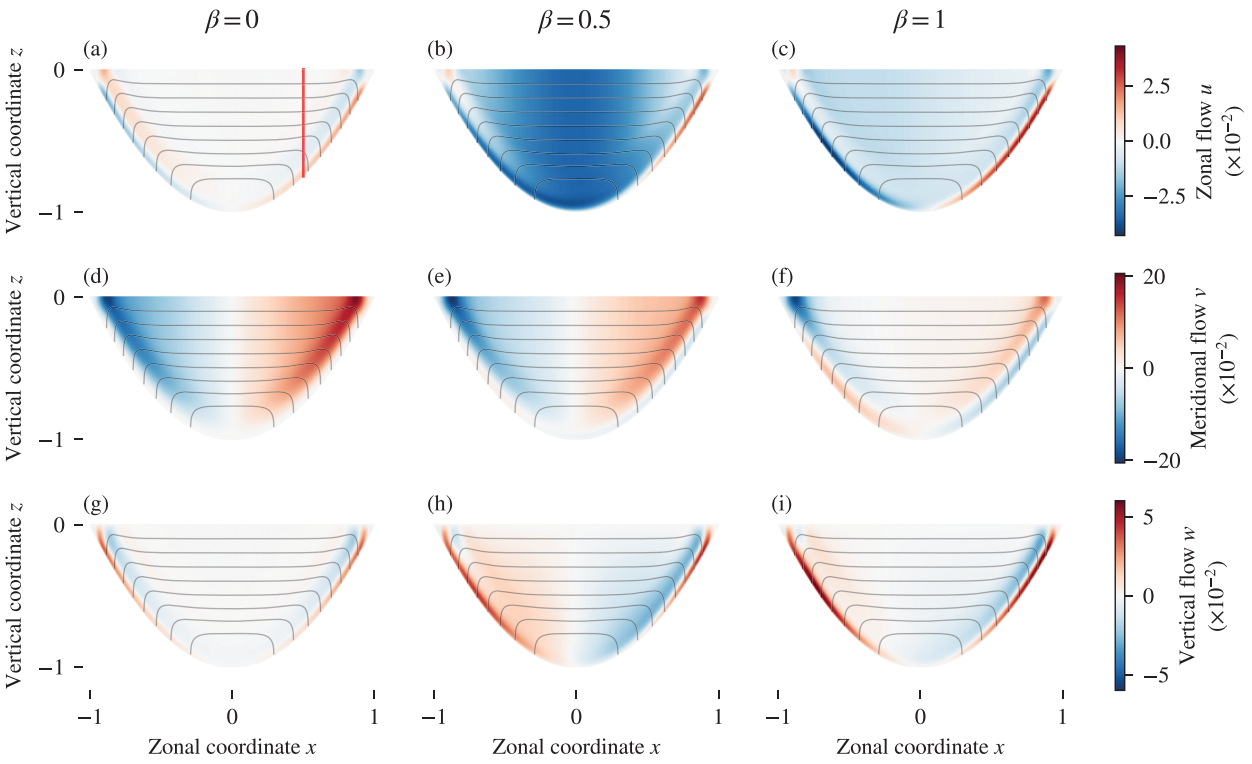

FIG. 4. Zonal sections at $y = 0$ of velocity components (colors) and isopycnals (gray lines) at $t = 10^{-2}$ for (left) $\beta = 0$, (center) $\beta = 0.5$, and (right) $\beta = 1$. The velocity components are organized by row: (top) zonal flow u, (middle) meridional flow v, and (bottom) vertical flow w. The red line in (a) indicates the location of profiles in Fig. 5.

this buoyancy field for the three cases outlined in Fig. 3, starting with the simplest case of an f plane.

b. Circulation on an f plane

On an f plane, by symmetry, the dynamics are equivalent for any slice through the origin. As discussed in the introduction, this along-slope invariance allows us to apply the theory built up in PC22 and PC23 to determine the local response. In particular, this means that the vertically integrated zonal velocity,

$$U \equiv \int_{-H}^{0} u \, dz, \tag{18}$$

along a zonal section through $y = 0$ (red line in Fig. 3) must vanish. Along this zonal section, the flow field exhibits the BL upwelling and interior downwelling characteristic of bottom-enhanced mixing (Figs. 4a,g). The transport constraint, by the meridional momentum balance [(10)] and the along-slope symmetry, implies that the meridional (along slope) shear $\partial_z v$ at the bottom must vanish. This, in turn, implies weak near-bottom flow, such that the thermal wind shear in the mixing layer leads to strong meridional flow in the interior (Fig. 4d). These dynamics are well described by the local theory, as showcased in Fig. 5 for a particular profile taken at $x = 0.5$ and $y = 0$ (red dot in Fig. 3). In section 4, this local model will be described and generalized in detail, but for now the transport-constrained one-dimensional model from PC22 is a sufficient mental picture.

As we make more explicit in section 4, the circulation in general must satisfy a barotropic vorticity equation. For the symmetric buoyancy field considered here, and in the absence of a wind stress, this implies free leading-order barotropic flow along closed f/H contours. On an f plane, this simply means that fluid columns must remain at a constant depth as they circumnavigate the basin. Defining a barotropic streamfunction Ψ, such that

$$-\frac{\partial \Psi}{\partial y} = U \quad \text{and} \quad \frac{\partial \Psi}{\partial x} = V, \tag{19}$$

where U is as defined in (18) and $V \equiv \int_{-H}^{0} v \, dz$, this implies that $\Psi = \Psi(H)$ (Fig. 6). The strength of this along-slope barotropic circulation is set by the amount of thermal wind shear over the mixing layer (see section 4 and appendix C for details). Specifically, as we will see in (42), the magnitude of Ψ is linearly proportional to the thickness of the mixing layer, the strength of the cross-slope buoyancy gradient within it, and the depth of the fluid column.

c. Circulation on a β plane

On a β plane, the f/H contours shift southward, breaking the axial symmetry that was present on the f plane and therefore invalidating the model for the local response based on

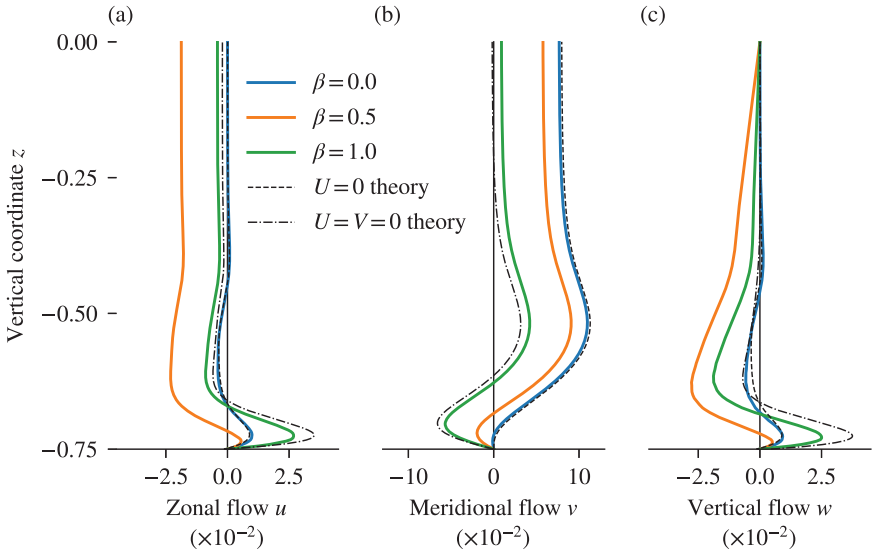

FIG. 5. Vertical profiles of (a) zonal u, (b) meridional v, and (c) vertical w flow components from the 3D model inversion (solid) for $\beta = 0$, 0.5, and 1 at $x = 0.5$, $y = 0$, and $t = 10^{-2}$. The second-order accurate local models for $U = 0$ and $U = V = 0$ (modified for an aspect ratio of 1/2; see appendixes B and C) are shown in dashed and dashed–dotted lines, respectively.

along-slope symmetry. We consider two cases: $\beta = 0.5$ and $\beta = 1$, with the former having closed f/H contours and the latter having open contours (Figs. 3b,c). As alluded to in the introduction, these two cases lead to dramatically different local- and basin-scale responses to the mixing-generated buoyancy field.

For closed f/H contours ($\beta = 0.5$), the magnitude of the barotropic circulation is comparable to that of the f-plane case (Fig. 6b). The streamfunction is very nearly a function of f/H, with a slight perturbation toward the western side of the basin. Looking again at a zonal section through $y = 0$, the interior meridional flow is similar to the f-plane case, with a slight barotropic shift toward zero in the interior (Fig. 4e). This is especially clear in the vertical profile at $x = 0.5$ and $y = 0$ (Fig. 5b). Because the f/H contours are no longer meridional along this zonal section, the along-contour transport constraint allows for a substantially enhanced zonal (cross isobath) flow (Figs. 4b and 5a). The zonal circulation in the interior of this section can best be understood by considering the stretching and squashing of fluid columns to conserve vorticity. Since f increases with y, fluid columns moving northward on the eastern side of the basin must stretch by moving toward deeper waters to the west to keep f/H constant. This explains the westward and downwelling interior flow on this side of the basin (Figs. 4b,h). On the other hand, fluid columns moving southward on the western side of the basin must squash by moving toward shallower waters, leading to westward and upwelling interior flow. More precisely, the interior vertical flow (Fig. 5c) is, to leading order, consistent with frictionless vorticity conservation, $f\partial_z w = \beta v$.

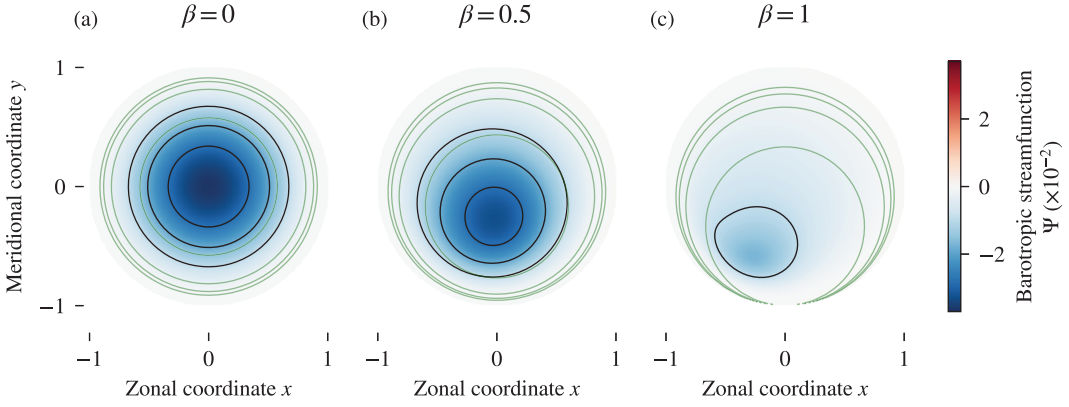

FIG. 6. Barotropic streamfunction Ψ (colors and black contours) at $t = 10^{-2}$ for (a) $\beta = 0$, (b) $\beta = 0.5$, and (c) $\beta = 1$. Negative values imply counterclockwise flow. For reference, the f/H contours from Fig. 3 are overlaid in green.

The circulation completely changes once f/H contours open. As before, the leading-order barotropic flow is directed along f/H contours, but this time these contours encounter the boundary, where the flow must be zero. The magnitude of the barotropic circulation is, therefore, considerably reduced (Fig. 6c). The near-zero transport throughout the domain provides a constraint that decouples the local response from the basinwide circulation. Unlike the model for the local response in the f-plane case, here both U and V must vanish at leading order. This model for the local response, described in section 4 and appendixes B and C, captures the qualitative vertical structure of the flow at $x = 0.5$ and $y = 0$, with quantitative errors to be expected given that the net transport is not exactly zero in the full inversion (Fig. 5). This constraint on the net transport has important implications for the vertical structure of the circulation. With the thermal wind shear unchanged, the meridional flow in the interior must shift to satisfy $V = 0$ (Figs. 4f and 5b). This generates a larger shear near the bottom, thereby enhancing the upslope BL transport (Figs. 4c,i and 5a,c). If buoyancy advection were allowed, this stronger BL upwelling than the f-plane case would be more efficient at restratifying the mixing layer, as we discuss further in section 5. To compensate for this BL transport and ensure that that $U \approx 0$, the zonal flow in the interior is weakly westward in balance with a barotropic meridional pressure gradient.

4. Theory for the flow inversion

The phenomenology exhibited in the previous section shows that, for a fixed buoyancy field, the circulation resulting from the PG inversion varies substantially depending on the underlying f/H contours. For open contours, the barotropic circulation vanishes at leading order, rendering the leading-order local response independent of any global context. For closed contours, on the other hand, a leading-order along-contour barotropic flow develops. This transport constrains the local response, whose bottom stress curl then provides a sink of barotropic vorticity so that, in general, the two problems must be solved simultaneously. For the f-plane case, however, the along-slope symmetry provided enough of a constraint to allow us to describe the local response independently with the model derived in PC22. In this section, we describe the mathematical formalism of these results, clarifying how the local and barotropic responses are coupled and deriving asymptotically accurate analytical expressions.

a. Barotropic vorticity conservation

Turbulent mixing of buoyancy in the abyss generates a local flow response that must reckon with the basinwide circulation. The barotropic circulation may be described by the barotropic vorticity equation, derived by integrating the horizontal momentum equations [(9) and (10)] over the water column and then cross differentiating (e.g., Pedlosky 1979; Vallis 2017):

$$-J\left(\frac{f}{H}, \Psi\right) = -J\left(\frac{1}{H}, \gamma\right) + \mathbf{z}\cdot\left(\nabla\times\frac{\boldsymbol{\tau}}{H}\right) - \varepsilon^2\mathbf{z}\cdot\nabla\times\left(\frac{\nu}{H}\frac{\partial\mathbf{u}}{\partial z}\bigg|_{-H}\right), \tag{20}$$

where $J(A, B) = \partial_x A\partial_y B - \partial_y A\partial_x B$ is the Jacobian operator. For a closed simply connected domain like the bowl considered in this study, the boundary condition is $\Psi = 0$. The first term on the right-hand side depends on both the topography and the three-dimensional structure of the buoyancy field through $\gamma = -\int_{-H}^{0} zb\,dz$ and is therefore often called the JEBAR term (Sarkisyan and Ivanov 1971; Schulman 1975). For our simple diffusion case, $\gamma = \gamma(H)$, so that JEBAR is zero.

Equation (20) can be interpreted as a conservation equation for the "tracer" Ψ advected by the "flow" f/H and with "sources" and "sinks" on the right-hand side (e.g., Welander 1968; Salmon 1998; Vallis 2017). This tracer analogy helps explain the qualitative difference between the open- and closed-contour inversions (Fig. 6). For closed f/H contours, the streamfunction can flow along a closed loop, gaining "concentration" from the source terms along the way. This is how the f plane and $\beta = 0.5$ simulations could maintain such strong barotropic circulations (e.g., Hallberg and Rhines 1996). For $\beta = 1$, however, the contours open, and any concentration acquired while "flowing" in the interior will be lost at the boundary. In the inversions shown above, the only source term is the bottom stress curl, which is itself a part of the solution. For closed contours, this frictional term can become large outside a lateral boundary layer, whereas open contours produce lateral (western) boundary layers with friction remaining small in the interior.

A closed description requires an expression for the bottom stress curl term in (20), where the barotropic circulation explicitly couples to the local response. In the classic Stommel (1948) model, the bottom stress is simply taken to be proportional to the vertically integrated transport; taking its curl then yields a term proportional to the horizontal Laplacian of Ψ, adding a lateral diffusion term to the tracer analogy. More physically, Ekman theory should be applied to the bottom boundary layer, such that the bottom stress depends on the near-bottom geostrophic flow. Because the near-bottom geostrophic flow depends on both the barotropic circulation and the baroclinic shear, this couples the barotropic problem to the local response to mixing. This theory is developed over the next two sections.

b. The local response to mixing

The local response can be determined by solving the frictional thermal wind relations, which arise from differentiating the momentum equations [(9) and (10)] in z and substituting hydrostatic balance [(11)]:

$$-f\frac{\partial v}{\partial z} = -\frac{\partial b}{\partial x} + \varepsilon^2\frac{\partial^2}{\partial z^2}\left(\nu\frac{\partial u}{\partial z}\right), \tag{21}$$

$$f\frac{\partial u}{\partial z} = -\frac{\partial b}{\partial y} + \varepsilon^2\frac{\partial^2}{\partial z^2}\left(\nu\frac{\partial v}{\partial z}\right). \tag{22}$$

All variables, including f and ν, remain nondimensional. Given the horizontal buoyancy gradients, (21) and (22) define a

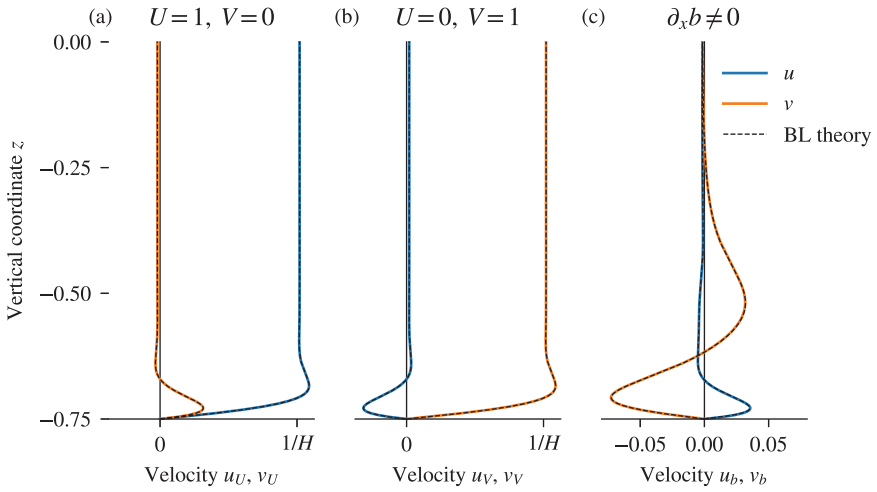

FIG. 7. Solutions to the frictional thermal wind equations [(21) and (22)] for cases with (a) zonal transport only, (b) meridional transport only, and (c) no transport with a zonal buoyancy gradient taken from the bowl simulation at $x = 0.5$, $y = 0$, and $t = 10^{-2}$ (see Fig. 1). These solutions are labeled with the subscripts U, V, and b, respectively, as in (25) and (26). Second-order accurate BL theory solutions (see appendix B) are shown in black dashed lines. Parameters are as in the full inversion at $x = 0.5$ and $y = 0$ ($\varepsilon = 2 \times 10^{-2}$, $f = 1$, $\nu = 1$, $H = 0.75$) with horizontal viscous terms ignored.

set of two coupled second-order ordinary differential equations in z for the shear of the horizontal flow $(\partial_z u, \partial_z v)$. The first set of boundary conditions is due to the wind stress ($\varepsilon^2 \nu \partial_z u = \tau^x$ and $\varepsilon^2 \nu \partial_z v = \tau^y$ at $z = 0$), while the second set arises from the barotropic transport constraint:

$$-\int_{-H}^{0} z \frac{\partial u}{\partial z}\, dz = U \quad \text{and} \quad -\int_{-H}^{0} z \frac{\partial v}{\partial z}\, dz = V, \tag{23}$$

coupling the problem to the barotropic vorticity equation [(20)]. Since $\mathbf{u} = 0$ at $z = -H$, the horizontal flow can easily be determined from the shear by integrating upward: $u(z) = \int_{-H}^{z} \partial_z u(z')\, dz'$ and $v(z) = \int_{-H}^{z} \partial_z v(z')\, dz'$. The vertical flow can be determined by cross differentiating the horizontal momentum equations [(9) and (10)] and applying continuity [(12)], which yields the frictional vorticity balance,

$$\beta v = f \frac{\partial w}{\partial z} + \varepsilon^2 \frac{\partial}{\partial z}\left(\nu \frac{\partial \zeta}{\partial z}\right), \tag{24}$$

where $\zeta = \partial_x v - \partial_y u$ is the relative vorticity. From this relation, it is clear that the local interior vertical velocity reflects the stretching or squashing needed to conserve potential vorticity of the fluid column as it moves across a meridional planetary vorticity gradient. Near the boundaries, where the friction term dominates, horizontal variations in the local response yield Ekman pumping and suction.

Solutions to (21) and (22) are well understood from standard Ekman theory (e.g., Ekman 1905; Pedlosky 1979; Vallis 2017). For a purely zonal transport with no horizontal buoyancy gradients, the flow is constant in the interior with $u = U/H$ and $v = 0$ and follows a classic Ekman spiral to zero in the bottom BL (Fig. 7a). For $f > 0$, the positive zonal transport spirals counterclockwise, generating a small, positive meridional transport in the BL. Likewise, for a positive meridional transport, the constant interior flow $u = 0$ and $v = V/H$ spirals near the bottom such that a small, negative zonal BL transport is created (Fig. 7b). Finally, when no net transport is allowed but a buoyancy gradient in x is present due to turbulent mixing on a slope, the shear in the meridional flow satisfies thermal wind in the interior (Fig. 7c). The constraint that $V = 0$ then implies a nonzero interior flow at the top of the bottom BL, leading to an Ekman spiral with positive zonal transport in the BL.

These hypothetical profiles already help to explain the qualitative differences between the vertical structure of the flow from the inversions shown in the previous section. By linearity of the baroclinic equations [(21) and (22)], the full flow within any vertical column in the domain may be thought of as a linear combination of the solutions in Fig. 7. In other words, if we call (u_U, v_U) and (u_V, v_V) the local responses for no horizontal buoyancy gradients and purely zonal (Fig. 7a) or meridional (Fig. 7b) transport, respectively, and (u_b, v_b) the baroclinic solution with no net transport (e.g., Fig. 7c for $x = 0.5$, $y = 0$, and $t = 10^{-2}$ from the bowl simulation), then the full solution may be written as

$$u = U u_U + V u_V + u_b, \tag{25}$$

$$v = U v_U + V v_V + v_b. \tag{26}$$

Given the barotropic streamfunction from Fig. 6 and the one-dimensional solutions u_U, v_U, u_V, v_V, u_b, and v_b shown in Fig. 7, we can infer the local flow profiles for each of the three bowl simulations. These descriptions should be compared with the actual flow profiles at this location and time shown in Fig. 5. For the case with open f/H contours ($\beta = 1$), the

barotropic transport is negligible throughout the domain (Fig. 6c), so the profiles mostly resemble u_b and v_b alone. For closed contours, on the other hand, the barotropic transport is large (Figs. 6a,b), leading to modifications due to the transport responses u_U, v_U, etc. On the f plane, for example, $U = 0$ and V is large and positive at this point. Since $Vu_V < 0$ in the BL and $Vv_V > 0$ in the interior, this leads to a reduction in the upslope BL transport and a strong along-slope flow in the interior. For $\beta = 0.5$, the meridional transport is still large and positive while the zonal transport is slightly negative. Thus, the contribution from Uu_U leads to a westward barotropic flow in the interior.

This formulation of the local problem is generally applicable, with the integral conditions [(23)] describing exactly how the local response is constrained by the barotropic problem [(20)]. Similarly, when along-slope symmetry is present, such as in the f-plane case in the bowl geometry, the barotropic problem can be sufficiently simplified to enable an explicit calculation of the local response. Taking x and y to be the local cross- and along-slope directions, neglecting along-slope variations in the barotropic vorticity equation [(20)] implies

$$\frac{\partial}{\partial x}\left(\frac{\nu}{H}\frac{\partial v}{\partial z}\bigg|_{-H}\right) = 0. \tag{27}$$

Integrating in x from the center of the domain, where the flow must vanish by symmetry, this reduces to the requirement that the along-slope shear vanishes everywhere along the bottom:

$$\frac{\partial v}{\partial z} = 0 \quad \text{at} \quad y = 0, \quad z = -H. \tag{28}$$

The same conclusion can be reached by integrating the y-momentum equation from $z = -H$ to $z = 0$, assuming $\partial_y p = 0$ and $U = 0$ (PC22). The constraint in (28) then replaces the along-slope integral boundary condition in (23), and the cross-slope transport is set to zero by the symmetry described above. This local model is mathematically equivalent to the streamfunction formulation of the dynamics in the x–z plane from PC22, but it more naturally generalizes to the three-dimensional problem. If one assumes a uniform bottom slope θ, the horizontal buoyancy gradient becomes $\partial_x b = -\partial_z b \tan\theta$, and the vertical flow is simply $w = u\tan\theta$, as in the standard one-dimensional models (see appendixes A and B).

c. Boundary layer theory

The barotropic and local problems outlined in the previous two sections form a complete description of the PG inversion. The two must be solved together, with the solution to the local problem feeding into the bottom-stress-curl sink term in the barotropic vorticity equation [(20)] and the barotropic solution appearing in the integral constraint [(23)] of the local inversion [(21) and (22)]. In this section, we use standard Ekman BL theory (e.g., Pedlosky 1979; Vallis 2017) to arrive at an analytical expression for the bottom stress, allowing us to explicitly describe how the local response couples to the basinwide dynamics. In the following, we describe the salient results of the BL theory; we leave the details in appendix B.

We split the flow into an interior contribution $\mathbf{u}_I$, which varies slowly in z, and bottom and surface BL corrections $\mathbf{u}_B$ and $\mathbf{u}_S$, respectively, which ensure boundary conditions are satisfied and have appreciable magnitude in thin BLs only. The interior solution is then, to $O(\varepsilon)$, in thermal wind balance:

$$f\frac{\partial v_I}{\partial z} = \frac{\partial b}{\partial x} \quad \text{and} \quad f\frac{\partial u_I}{\partial z} = -\frac{\partial b}{\partial y}. \tag{29}$$

In the absence of a buoyancy gradient, the flow in the interior is constant, consistent with both profiles in Figs. 7a and 7b and u in Fig. 7c (where $\partial_y b = 0$). To satisfy the no-flow boundary condition at the bottom, this flow is brought to zero by friction in a classic Ekman spiral, with coefficients set by the (yet to be determined) interior flow at the top of the bottom BL:

$$u_B = -e^{-q\bar{z}}(u_I|_{-H}\cos q\bar{z} + v_I|_{-H}\sin q\bar{z}), \tag{30}$$

$$v_B = -e^{-q\bar{z}}(v_I|_{-H}\cos q\bar{z} - u_I|_{-H}\sin q\bar{z}). \tag{31}$$

The solution is written in terms of the stretched vertical coordinate $\bar{z} = (z + H)/\varepsilon$, and $q^{-1} = \sqrt{2\nu|_{-H}/f}$ is the bottom BL thickness in this coordinate. With $b = 0$ at $z = 0$, the shear of the interior velocities [(29)] is zero at the surface, automatically satisfying the surface boundary condition for no wind stress. If a nonzero wind stress is allowed, an $O(\varepsilon^{-1})$ Ekman spiral BL correction at the surface $\mathbf{u}_S$ must be present as well.

The Ekman spiral in the bottom BL [(30) and (31)] generates considerable shear near the bottom, providing a frictional sink of barotropic vorticity. To derive an explicit formula for the curl of this bottom stress, we must first determine the interior flow at the top of the BL $u_I|_{-H}$ and $v_I|_{-H}$. This can be done by considering the contributions of the interior and BL components to the vertically integrated transport:

$$U = U_I + U_S + \varepsilon U_B \quad \text{and} \quad V = V_I + V_S + \varepsilon V_B. \tag{32}$$

Due to the thinness of the surface and bottom BLs, their integrals pick up a factor of ε, but since the surface BL correction is of $O(\varepsilon^{-1})$, its integral contribution is of $O(1)$. Neglecting the $O(\varepsilon)$ contributions from the bottom BL in (32) and solving for the interior flow at the top of the bottom BL yields

$$u_I|_{-H} = \frac{U}{H} - \frac{1}{fH}\int_{-H}^{0} z\frac{\partial b}{\partial y}\,dz - \frac{\tau^y}{fH}, \tag{33}$$

$$v_I|_{-H} = \frac{V}{H} + \frac{1}{fH}\int_{-H}^{0} z\frac{\partial b}{\partial x}\,dz + \frac{\tau^x}{fH}. \tag{34}$$

With these constants determined, it is now possible to write down the bottom stress due to the BL correction [(30) and (31)]:

$$\varepsilon^2\nu\frac{\partial u_B}{\partial z}\bigg|_{-H} = \varepsilon\nu|_{-H}q\left[\frac{U - V}{H} - \frac{1}{fH}\int_{-H}^{0} z\left(\frac{\partial b}{\partial x} + \frac{\partial b}{\partial y}\right)dz - \frac{\tau^x + \tau^y}{fH}\right], \tag{35}$$

$$\varepsilon^2\nu\frac{\partial v_B}{\partial z}\bigg|_{-H} = \varepsilon\nu|_{-H}q\left[\frac{U + V}{H} + \frac{1}{fH}\int_{-H}^{0} z\left(\frac{\partial b}{\partial x} - \frac{\partial b}{\partial y}\right)dz + \frac{\tau^x - \tau^y}{fH}\right]. \tag{36}$$

This $O(\varepsilon)$ contribution is the dominant term in the full stress. Equations (35) and (36) explicitly separate the contributions

to the bottom stress in terms of three physical sources: 1) the barotropic transports, 2) the full-column buoyancy gradients, and 3) the wind stress. The latter two terms are external forcings to the problem, while the barotropic transports couple the local flow to the basin-scale circulation.

Plugging these analytical expressions for the bottom stress into the barotropic vorticity equation [(20)] yields the following closed equation for the barotropic streamfunction:

$$\varepsilon\nabla_\perp\cdot\left(\frac{r}{H}\nabla_\perp\Psi\right)-J\left(\frac{f+\varepsilon r}{H},\Psi\right)=-J\left(\frac{1}{H},\gamma\right)+\mathbf{z}\cdot\left(\nabla\times\frac{\boldsymbol{\tau}}{H}\right)-\varepsilon\mathcal{B}-\varepsilon\mathcal{T}, \tag{37}$$

where $\nabla_\perp=(\partial_x,\partial_y)$ is the horizontal gradient operator,

$$\mathcal{B}=\frac{\partial}{\partial x}\left[\frac{r}{fH}\int_{-H}^{0}z\left(\frac{\partial b}{\partial x}-\frac{\partial b}{\partial y}\right)dz\right]+\frac{\partial}{\partial y}\left[\frac{r}{fH}\int_{-H}^{0}z\left(\frac{\partial b}{\partial x}+\frac{\partial b}{\partial y}\right)dz\right] \tag{38}$$

is the curl of the bottom stress due to baroclinicity, and

$$\mathcal{T}=\frac{\partial}{\partial x}\left(\frac{\tau^x+\tau^y}{fH}\right)-\frac{\partial}{\partial y}\left(\frac{\tau^y-\tau^x}{fH}\right) \tag{39}$$

is the curl of wind-induced bottom stress. Because the first terms in the equations for the bottom stresses [(35) and (36)] are proportional to U and V, a Laplacian term appears just as in the Stommel theory, with the diffusion coefficient $r/H=\nu|_{-H}q/H^2$ dependent on the thickness of the bottom BL. In contrast with the Stommel model, there is also a cross term $\varepsilon J(r/H,\Psi)$, applying an $O(\varepsilon)$ modification to the "advection" term $J(f/H,\Psi)$ (e.g., Rattray 1982). The more important changes come from the other two terms in the bottom stresses: The term due to the baroclinic buoyancy response and the term due to the bottom return flow from the wind stress forcing contribute $O(\varepsilon)$ sources to Ψ.

Making use of the fact that $\varepsilon\ll 1$, we can further describe the physics of the barotropic circulation in terms of its expansion in ε, defining $\Psi=\Psi_0+\varepsilon\Psi_1+\cdots$. The leading-order balance in (37) is then simply

$$-J\left(\frac{f}{H},\Psi_0\right)=-J\left(\frac{1}{H},\gamma\right)+\mathbf{z}\cdot\left(\nabla\times\frac{\boldsymbol{\tau}}{H}\right)=0, \tag{40}$$

where the last equality is true in our inversions with no wind stress and $\gamma=\gamma(H)$. This confirms our intuition that the leading-order barotropic streamfunction is constant along f/H contours: $\Psi_0=\Psi_0(f/H)$ (e.g., Rattray 1982; Mertz and Wright 1992). The source terms due to the curl of the bottom stress come into play at $O(\varepsilon)$:

$$\nabla_\perp\cdot\left(\frac{r}{H}\nabla_\perp\Psi_0\right)-J\left(\frac{r}{H},\Psi_0\right)-J\left(\frac{f}{H},\Psi_1\right)=\mathcal{B}+\mathcal{T}. \tag{41}$$

For open contours, $\Psi_0(f/H)$ must be identically zero due to the boundary condition $\Psi_0=0$ at the coast, explaining the destruction of the leading-order streamfunction for the $\beta=1$ inversion (Fig. 6c). The strength of the circulation is then set at the next order by $\mathcal{B}$ and $\mathcal{T}$, with the addition of a lateral boundary layer to satisfy the boundary condition, as in the standard Stommel theory (Veronis 1966). The theoretical profiles in Fig. 5 simply assume $U=V=0$, which is true to leading order and fully decouples the local response from the barotropic circulation. For closed contours, $\Psi_0(f/H)$ is nonzero and can, in general, be determined by integrating (41) along f/H contours to remove the Ψ_1 term. This leads to a second-order ODE for $\Psi_0(f/H)$ with a forcing due to the integral of $\mathcal{B}+\mathcal{T}$ on the RHS.

When along-slope symmetry is present, as in our f-plane case, the along-slope barotropic transport can be directly computed from the model for the local response described above and in appendix C. Applying the constraints $\partial_y b=0$, $U=0$, and $\partial_z v|_{-H}=0$ and solving for V yields,

$$\frac{\partial\Psi_0}{\partial x}=-\frac{1}{f}\int_{-H}^{0}z\frac{\partial b}{\partial x}\,dz\quad\text{and}\quad\frac{\partial\Psi_1}{\partial x}=-\frac{H}{fq}\frac{\partial b}{\partial x}\bigg|_{-H}. \tag{42}$$

For a full derivation out to $O(\varepsilon^2)$, see appendix C. Physically, the leading-order term represents thermal wind shear integrated over the column. In our simulations, this shear is only nonnegligible over the mixing layer, suggesting that

$$\Psi_0(0)\approx-\frac{h\Delta_x b}{f}\int_0^1 H\,dx=-\frac{2h\Delta_x b}{3f}, \tag{43}$$

where $\Delta_x b$ is the average horizontal buoyancy gradient over the mixing layer and h is the scale height of κ, taken to be 0.1 in (17). With $f=1$ and setting $\Delta_x b=1$ (cf. Fig. 1d), (43) would imply $\Psi_0\approx-7\times10^{-2}$ at $x=0$. In this case, therefore, the leading-order contribution to the streamfunction is much smaller than unity and not much larger than $\varepsilon=2\times10^{-2}$, implying that the first-order correction in (42) plays an important quantitative role (Fig. 8). This correction is due to a barotropic $O(\varepsilon)$ interior flow that sets up a bottom Ekman layer whose along-slope shear must be constrained to zero at the bottom. Similarly, to achieve quantitative agreement in Fig. 5, the profiles for the local responses are computed out to $O(\varepsilon^2)$ (see appendixes B and C).

5. Discussion

The buoyancy distribution of the abyssal ocean in steady state is set by a balance between diapycnal advection and diapycnal mixing (Munk 1966). The advecting flow is itself a function of this buoyancy field, and, in this work, we chose to focus our attention on this dependence in the context of the PG approximation. In the "strong diffusion regime," where $\mu\varrho\sim\varepsilon^2$, this yields a full description of the circulation: The buoyancy evolves according to simple diffusion, and the flow passively varies according to the PG inversion of this field. Restricting ourselves to this very basic dynamics allowed us to make progress in understanding the generalizations of previous theories for the local response to mixing. It is worth noting that, assuming one somehow knew the steady-state buoyancy field from the advection–diffusion problem, the analysis presented here would apply to the steady-state flow field. Without a complete

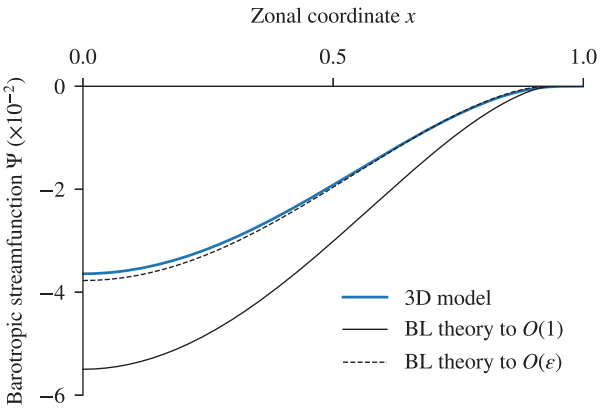

FIG. 8. Comparison of the barotropic streamfunction Ψ at $t = 10^{-2}$ and $y = 0$ between the 3D f-plane inversion and the local model assuming along-slope symmetry [(42)]. The modifications to the local model described in appendix C are applied to partially account for the added viscous terms in the 3D model.

understanding of how this flow is determined, however, it would be impossible to know how the buoyancy field arrived at that steady state to begin with. This paper therefore represents one important step in developing a full theory for the abyssal circulation, with the next being to consider the feedback of this flow onto the buoyancy field.

Some speculation for how advection could shape the buoyancy field, given the flow inversions presented here, is possible. For instance, the enhanced BL upwelling for open f/H contours (Figs. 4i and 5c) could encounter a negative feedback once it is allowed to interact with the hydrography. This transport of dense water up the slope would work to restratify the abyssal mixing layer even without a parameterization of restratification due to baroclinic eddies (Wenegrat et al. 2018; Callies 2018). This flattening of isopycnals will, in turn, reduce the thermal wind shear above the BL, weakening the BL transport. This negative feedback on the BL transport could be particularly relevant given the ubiquity of open f/H contours in the real ocean (Fig. 2). The larger interior vertical velocities for β-plane inversions (Figs. 4h,i and 5c) would also modify the interior stratification with advection allowed. The pattern of downwelling on the eastern side and upwelling on the western side of the basin for the zonal section at $y = 0$ would work to generate a positive zonal buoyancy gradient and hence poleward shear in the interior meridional flow. This flow must, in turn, conserve vorticity, perturbing the vertical velocities and likely generating westward-propagating long Rossby waves. These Rossby waves would then allow for communication between the eastern and western sides of the basin, playing an important role in setting up a western boundary current in the early stages of spinup (e.g., Pedlosky 1965; Rhines 1975).

Ultimately, the goal should be to describe these dynamics in terms of BL–interior communication to better understand the role that bottom-enhanced mixing plays in shaping the abyssal circulation. The BL theory in PC23 builds a foundation for this theory by considering the case with along-slope symmetry. This theory illustrates how upslope BL transport supplies a downward flux of buoyancy that the interior feels as an effective bottom boundary condition. As the cross-slope stratification at the top of the BL evolves, so does the BL transport, providing an avenue for exchange. This description should carry over to the more general case, with the local response now coupled to the barotropic vorticity equation as discussed here. While the interior dynamics may evolve on a faster time scale, supporting Rossby waves, the BLs should remain quasi steady, again setting an effective bottom boundary condition on the interior.

In this paper, we only show numerical inversions for the simple case of no wind stress and a symmetric buoyancy field in a simple basin geometry. The theory is general, however, allowing us to reason about how the circulation would change under different scenarios without explicitly computing the inversion. In general, the wind stress curl and JEBAR terms provide leading-order sources/sinks of barotropic vorticity in (40). If these terms are nonzero, a leading-order barotropic circulation could be supported even in the open f/H contour case. The wind-forced circulation, however, should be largely confined to the thermocline, reducing its impact on the abyssal circulation, at least in subtropical regions (Luyten et al. 1983). We put our focus on the abyssal circulation powered by bottom-enhanced mixing, but its interplay with the wind-forced circulation, especially in subpolar regions, could be studied using the same framework.

As a final caveat, we note that the analytical theory presented in the main text of this work assumes no horizontal diffusion and no diffusion in the vertical momentum equation, while the numerical solutions to the PG equations do include these terms for stability. Over a uniform slope, these terms contribute a factor of $(1 + \alpha^2 \tan^2\theta)^{3/4}$ modification to the BL scale q^{-1} (appendixes A and C). While this leads to a slight quantitative modification to the flow, the qualitative physics remain unchanged. This correction is included in the BL solutions presented in Figs. 5 and 8 to more directly compare with the three-dimensional model, although slight errors are still expected due to curvature in the slope. The BL solutions in Fig. 7 do not require this modification, as there the local response is computed directly from (21) and (22) without these diffusion terms.

6. Conclusions

Our understanding of how observed bottom-enhanced mixing shapes the global abyssal ocean circulation has been guided by theories focused on the local dynamics above slopes (e.g., Phillips et al. 1986; McDougall 1989; Garrett 1991; Dell and Pratt 2015; Holmes et al. 2018; Callies and Ferrari 2018; Drake et al. 2020). In this work, we explored how this local response couples to the basin-scale barotropic circulation for a fixed buoyancy field under the PG approximation. While barotropic dynamics have been well understood since Welander (1968), their connection to the baroclinic response to mixing over sloping topography has not been fully appreciated. We found that the bottom stress curl of the local response forces the barotropic vorticity through three primary mechanisms: shear due to barotropic interior currents, baroclinicity of the buoyancy field, and

bottom return flow due to the wind stress. These terms drop out at leading order away from the coastline, yielding the standard balance between "advection" of Ψ along f/H contours and "sources" from JEBAR and the wind stress curl (e.g., Rattray 1982; Mertz and Wright 1992).

To focus on how the baroclinicity of the local response shapes the barotropic circulation, we considered the flow field resulting from zero wind stress and a buoyancy field that is a function of depth. The sources in the leading-order barotropic vorticity equations vanish in this case, implying that Ψ_0 must follow f/H contours. When these contours are closed, such as over large topographic features (e.g., the Argentine Basin; Fig. 2), a leading-order along-contour transport develops, with its magnitude set by the thermal wind shear over the mixing layer. On an f plane, this corresponds to an along-slope transport, and, for axisymmetric bathymetry, the local response is completely determined by the one-dimensional model of PC22. For open f/H contours, in contrast, Ψ_0 must be zero, decoupling the leading-order local response from the large-scale context.

This second case is more representative of the f/H contours in real ocean basins (Fig. 2) and has important implications for the influence of the BL on the interior circulation. Constraining the net transport of the local response to zero enhances the along-slope flow at the top of the BL, promoting the BL upwelling from $O(\varepsilon)$ to $O(1)$ compared to the response in the case of along-slope symmetry. Once allowed to advect buoyancy, this BL flow would more efficiently transport dense water up the slope, supplying a stronger effective buoyancy flux at the bottom felt by the interior (cf. PC23). Some combination of this enhanced BL upwelling and the transport due to submesoscale baroclinic eddies (Wenegrat et al. 2018; Callies 2018) is responsible for maintaining the stratification in the abyss.

Acknowledgments. This material is based upon work supported by the National Science Foundation under Grant OCE-2149080. H. G. P. thanks the Schmidt Academy for Software Engineering for additional funding and software advice, as well as the developers of Gridap.jl for assistance with using their package. We thank the two anonymous reviewers for their constructive feedback on the original manuscript.

Data availability statement. The PG inversions were computed using version 0.2.0 of the νPGCM, and the scripts for reproducing the figures are hosted at https://github.com/hgpeterson/PC_bowl_basin.

APPENDIX A

The PG Inversion with Nonzero Aspect Ratio

The nondimensional PG inversion, as it is presented in (9)–(12) in the main text, implicitly assumes a small aspect ratio and, hence, does not contain any viscous horizontal momentum transfer. This is an excellent assumption for the ocean, since, using the scales from section 2b, the aspect ratio is $\alpha \equiv H_0/L \sim 10^{-3}$. For numerical stability, however, we found it necessary to reintroduce these terms by artificially inflating the aspect ratio. This comes with the cost of quantitative errors, but the qualitative dynamics remain the same, as demonstrated in this appendix.

The PG inversion that our numerical model ultimately solves reads

$$-fv = -\frac{\partial p}{\partial x} + \varepsilon^2\left(\alpha^2\frac{\partial^2 u}{\partial x^2} + \alpha^2\frac{\partial^2 u}{\partial y^2} + \frac{\partial^2 u}{\partial z^2}\right), \tag{A1}$$

$$fu = -\frac{\partial p}{\partial y} + \varepsilon^2\left(\alpha^2\frac{\partial^2 v}{\partial x^2} + \alpha^2\frac{\partial^2 v}{\partial y^2} + \frac{\partial^2 v}{\partial z^2}\right), \tag{A2}$$

$$\frac{\partial p}{\partial z} = b + \varepsilon^2\alpha^2\left(\alpha^2\frac{\partial^2 w}{\partial x^2} + \alpha^2\frac{\partial^2 w}{\partial y^2} + \frac{\partial^2 w}{\partial z^2}\right), \tag{A3}$$

$$\nabla\cdot\mathbf{u} = 0. \tag{A4}$$

For $\alpha \neq 0$, horizontal diffusion terms are retained in the momentum equations. Crucially, hydrostatic balance is no longer exactly satisfied in (A3). This allows us to use classical finite-element techniques for Stokes flow, as described in the main text. For simplicity, we have set $\nu = 1$, as used throughout the paper.

To quantify the impact that artificially increasing α has on the inversions considered here, we consider the simple case of a uniform bottom slope in the x direction at a nondimensional angle θ with the horizontal. The dynamics in this case are fully described by a 1D model in the slope-following vertical direction, with the nonzero component of horizontal diffusive fluxes in this direction leading to modifications to the $\alpha = 0$ PC22 model. This yields a reasonable first approximation of aspect ratio effects given the skill of 1D theory in more general settings, as shown in the main text. To derive the 1D model, we define the transformation from Cartesian to slope-following coordinates as

$$\xi = x, \quad \eta = y, \quad \zeta = z - x\tan\theta \tag{A5}$$

(see PC22, Fig. A1, for a sketch).[A1] The contravariant velocity components under this coordinate transformation are then

$$u^\xi = u, \quad u^\eta = v, \quad u^\zeta = w - u\tan\theta, \tag{A6}$$

and the partial derivatives transform as

$$\frac{\partial}{\partial x} = \frac{\partial}{\partial \xi} - \tan\theta\frac{\partial}{\partial \zeta}, \quad \frac{\partial}{\partial y} = \frac{\partial}{\partial \eta}, \quad \frac{\partial}{\partial z} = \frac{\partial}{\partial \zeta}. \tag{A7}$$

Neglecting variations in planes parallel to the slope (the ξ and η directions) while still allowing for a cross-slope barotropic pressure gradient $\partial_x P$, the PG inversion with nonzero aspect ratio becomes

$$-fu^\eta = -\frac{\partial P}{\partial x} + b'\tan\theta + \Gamma^2\varepsilon^2\frac{\partial}{\partial \zeta}\left(\nu\frac{\partial u^\xi}{\partial \zeta}\right), \tag{A8}$$

[A1] The symbol ζ is here used as a vertical coordinate, not as the relative vorticity, as in the main text.

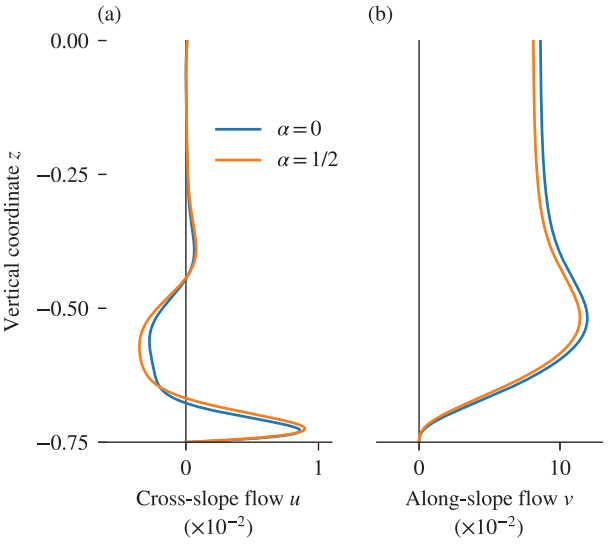

FIG. A1. Snapshot of (a) cross-slope flow u and (b) along-slope flow v satisfying the transport-constrained 1D equations [(A8)–(A10)] for aspect ratios $\alpha = 0$ and 1/2 and the same mixing-driven buoyancy field at $t = 10^{-2}$ used in the main text. The column depth $H = 0.75$ and local slope $\theta = \pi/4$ corresponding to the point $x = 0.5$ and $y = 0$ on the bowl, as in Fig. 5. In this case, the vertical velocity profile is the same as the cross-slope flow because $w = u\tan\theta$.

$$fu^{\xi} = \Gamma\varepsilon^2\frac{\partial}{\partial\zeta}\left(\nu\frac{\partial u^{\eta}}{\partial\zeta}\right), \tag{A9}$$

$$\int_{-H}^{0} u^{\xi}\,d\zeta = 0, \tag{A10}$$

where b' is the buoyancy perturbation from a background $b = z$. Equations (A8)–(A10) are derived from the more general form of (A1)–(A4) allowing for variations in ν, and they form the generalization of the (nondimensional) transport-constrained 1D inversion for $\alpha \neq 0$. The only differences to the $\alpha = 0$ model are the factors of $\Gamma = 1 + \alpha^2\tan^2\theta$ multiplying the flux terms. Physically, these factors come from the projection of the horizontal fluxes in the direction of the slope, with an extra factor of Γ in the ξ-momentum equation due to the nonhydrostatic part of $\partial_{\xi}p$.

Even for $\alpha = 1/2$, three orders of magnitude larger than that of the abyssal ocean, the 1D model solutions at $\theta = \pi/4$ (corresponding to $x = 0.5$ and $y = 0$ in the bowl, as in Fig. 5) are qualitatively similar to the $\alpha = 0$ case (Fig. A1). As expected, the factors of $\Gamma = 1.25$ on the friction terms lead to slight thickening of the BL (Fig. A1a). From BL theory, the new bottom Ekman layer thickness is $\delta = \Gamma^{4/3}\sqrt{2}\varepsilon$ (see appendix C). Somewhat more surprisingly, the interior along-slope flow is reduced for the $\alpha = 1/2$ case (Fig. A1b). This can be explained with BL theory, where we find that the asymptotic expansion of $\partial_x P \sim fv|_0$ in ε is

$$\frac{\partial P}{\partial x} = b'|_{-H}\tan\theta - \varepsilon\Gamma^{4/3}\sqrt{\frac{2\nu|_{-H}}{f}}\tan\theta + O(\varepsilon^2). \tag{A11}$$

The first term comes from the transport constraint, which forces the interior along-slope flow to be zero at the top of the BL. The $O(\varepsilon)$ correction comes from the fact that the shear in the $O(1)$ interior along-slope flow must balance the shear from the $O(\varepsilon)$ BL correction. Since $\Gamma^{4/3} \approx 1.3$ for $\alpha = 1/2$, the change in $\partial_x P$ between the two cases is about 10^{-2}, consistent with the change in $v|_0$ in Fig. A1.

APPENDIX B

BL Solution to the Frictional Thermal Wind Equations

This appendix contains the full derivation of the BL theory solution to the local inversion [(21) and (22)] described in section 4. As described in the main text, we split the flow into interior, surface BL, and bottom BL components $\mathbf{u}_I$, $\mathbf{u}_S$, and $\mathbf{u}_B$, respectively. We further expand these components in ε so that $\mathbf{u}_I = \mathbf{u}_{I0} + \varepsilon\mathbf{u}_{I1} + \varepsilon^2\mathbf{u}_{I2} + \cdots$ and $\mathbf{u}_B = \mathbf{u}_{B0} + \varepsilon\mathbf{u}_{B1} + \varepsilon^2\mathbf{u}_{B2} + \cdots$. As we will see below, the surface boundary condition $\varepsilon^2\nu\partial_z\mathbf{u}_{\perp} = \boldsymbol{\tau}$ requires that the leading-order surface BL correction be of $O(\varepsilon^{-1})$: $\mathbf{u}_S = \varepsilon^{-1}\mathbf{u}_{S-1} + \mathbf{u}_{S0} + \varepsilon\mathbf{u}_{S1} + \cdots$. In what follows, we determine the solutions for each component up to $O(\varepsilon^2)$, applying matching conditions between them to satisfy the boundary conditions and transport constraints. In the last subsection, we briefly outline how the vertical flow may be determined.

a. Leading-order solution

Starting with the interior equations,

$$-f\frac{\partial v_I}{\partial z} = -\frac{\partial b}{\partial x} + \varepsilon^2\frac{\partial^2}{\partial z^2}\left(\nu\frac{\partial u_I}{\partial z}\right), \tag{B1}$$

$$f\frac{\partial u_I}{\partial z} = -\frac{\partial b}{\partial y} + \varepsilon^2\frac{\partial^2}{\partial z^2}\left(\nu\frac{\partial v_I}{\partial z}\right), \tag{B2}$$

we immediately find that, to leading order, the horizontal flow is in thermal wind balance,

$$f\frac{\partial v_{I0}}{\partial z} = \frac{\partial b}{\partial x} \quad \text{and} \quad f\frac{\partial u_{I0}}{\partial z} = -\frac{\partial b}{\partial y}, \tag{B3}$$

as shown in (29) in the main text. To ensure that the transport constraints [(23)] are satisfied at each order, we must keep track of the vertically integrated transport due to each component of the flow. The transport due to this leading-order interior flow can be determined by integrating twice in the vertical and using integration by parts:

$$\int_{-H}^{0} u_{I0}\,dz = Hu_{I0}|_{-H} + \frac{1}{f}\int_{-H}^{0} z\frac{\partial b}{\partial y}\,dz \equiv U_{I0}, \tag{B4}$$

$$\int_{-H}^{0} v_{I0}\,dz = Hv_{I0}|_{-H} - \frac{1}{f}\int_{-H}^{0} z\frac{\partial b}{\partial x}\,dz \equiv V_{I0}, \tag{B5}$$

where the leading-order interior flow at the top of the BL $\mathbf{u}_{I0}|_{-H}$ is yet to be determined.

To determine the bottom BL correction, we transform (21) and (22) using the stretched vertical coordinate $\overline{z} = (z + H)/\varepsilon$

so that $\partial_z \to \varepsilon^{-1}\partial_{\overline{z}}$. The frictional terms are then promoted to $O(1)$, so, assuming the turbulent viscosity varies over a scale much larger than the bottom BL, the bottom BL flow satisfies

$$-f\frac{\partial v_B}{\partial \overline{z}} = \nu|_{-H}\frac{\partial^3 u_B}{\partial \overline{z}^3}, \tag{B6}$$

$$f\frac{\partial u_B}{\partial \overline{z}} = \nu|_{-H}\frac{\partial^3 v_B}{\partial \overline{z}^3}. \tag{B7}$$

Note that the buoyancy gradient terms are taken care of in the interior equations [(B1) and (B2)]. Upon integration in the vertical (keeping in mind that $\mathbf{u}_B \to 0$ as $\overline{z} \to \infty$) and substitution, (B6) and (B7) can be combined into a single, fourth-order ODE for u_B:

$$\frac{\partial^4 u_B}{\partial \overline{z}^4} + 4q_B^4 u_B = 0, \tag{B8}$$

where $q_B^{-1} = \sqrt{2\nu|_{-H}/f}$ is the bottom BL thickness in $\overline{z}$ coordinates. Since there are no factors of ε in this equation, it is true for each order of u_B. The leading-order bottom BL correction is therefore a classic Ekman spiral with coefficients determined by the bottom boundary condition $\mathbf{u}_{I0} = -\mathbf{u}_{B0}$:

$$u_{B0} = -e^{-q_B\overline{z}}(u_{I0}|_{-H}\cos q_B\overline{z} + v_{I0}|_{-H}\sin q_B\overline{z}), \tag{B9}$$

$$v_{B0} = -e^{-q_B\overline{z}}(v_{I0}|_{-H}\cos q_B\overline{z} - u_{I0}|_{-H}\sin q_B\overline{z}), \tag{B10}$$

corresponding to (30) and (31) in the main text. The vertical integral of this leading-order bottom BL correction picks up a factor of ε due to the thinness of the layer:

$$\varepsilon\int_0^\infty u_{B0}\,d\overline{z} = -\varepsilon\frac{u_{I0}|_{-H} + v_{I0}|_{-H}}{2q_B} \equiv \varepsilon U_{B1}, \tag{B11}$$

$$\varepsilon\int_0^\infty v_{B0}\,d\overline{z} = +\varepsilon\frac{u_{I0}|_{-H} - v_{I0}|_{-H}}{2q_B} \equiv \varepsilon V_{B1}. \tag{B12}$$

If a nonzero buoyancy gradient and/or wind stress is present at the surface, a BL will form there as well. In the stretched vertical coordinate $\hat{z} = z/\varepsilon$, we again arrive at a fourth-order ODE for u_S,

$$\frac{\partial^4 u_S}{\partial \hat{z}^4} + 4q_S^4 u_S = 0, \tag{B13}$$

this time with $q_S^{-1} = \sqrt{2\nu|_0/f}$. The surface stress boundary condition, split between the interior and BL components, is

$$\varepsilon\nu\frac{\partial u_S}{\partial \hat{z}} = \tau^x - \varepsilon^2\nu\frac{\partial u_I}{\partial z} \quad \text{and} \quad \varepsilon\nu\frac{\partial v_S}{\partial \hat{z}} = \tau^y - \varepsilon^2\nu\frac{\partial v_I}{\partial z} \tag{B14}$$

at $z = 0$. As alluded to above, this shows explicitly that a surface BL correction of $O(\varepsilon^{-1})$ is needed to balance the $O(1)$ wind stress. This correction must again be of the form

$$u_{S-1} = e^{q_S\hat{z}}(c_1\cos q_S\hat{z} + c_2\sin q_S\hat{z}), \tag{B15}$$

$$v_{S-1} = e^{q_S\hat{z}}(c_1\sin q_S\hat{z} - c_2\cos q_S\hat{z}), \tag{B16}$$

where the coefficients can be determined from the $O(1)$ surface boundary condition [(B14)], which yields

$$c_1 = \frac{\tau^x + \tau^y}{2\nu|_0 q_S} \quad \text{and} \quad c_2 = \frac{\tau^x - \tau^y}{2\nu|_0 q_S}. \tag{B17}$$

The vertical integral of the surface BL correction again picks up a factor of ε due to the thinness of the layer, but this cancels with the ε^{-1} order of the flow:

$$\int_{-\infty}^0 u_{S-1}\,d\hat{z} = +\frac{\tau^y}{f} \equiv U_{S0}, \tag{B18}$$

$$\int_{-\infty}^0 v_{S-1}\,d\hat{z} = -\frac{\tau^y}{f} \equiv V_{S0}, \tag{B19}$$

so this transport is ultimately of the same order as $\mathbf{U}_{I0}$ (Ekman 1905).

The leading-order solution to the local inversion is now fully characterized apart from the constants $u_{I0}\,|_{-H}$ and $v_{I0}|_{-H}$. These can be determined in terms of the barotropic transport $\mathbf{U}$ by combining the contributions from each of these components. Expanding the transport in ε so that $\mathbf{U} = \mathbf{U}_0 + \varepsilon\mathbf{U}_1 + \varepsilon^2\mathbf{U}_2 + \cdots$, we have the $O(1)$ balance

$$\mathbf{U}_0 = \mathbf{U}_{I0} + \mathbf{U}_{S0}, \tag{B20}$$

with $\mathbf{U}_{B1}$ contributing at the next order. Substituting the results from (B4), (B5), (B18), and (B19) into (B20) and solving for the interior velocities at the top of the bottom BL yields

$$u_{I0}|_{-H} = \frac{U_0}{H} - \frac{1}{fH}\int_{-H}^0 z\frac{\partial b}{\partial y}\,dz - \frac{\tau^y}{fH}, \tag{B21}$$

$$v_{I0}|_{-H} = \frac{V_0}{H} + \frac{1}{fH}\int_{-H}^0 z\frac{\partial b}{\partial x}\,dz + \frac{\tau^x}{fH}, \tag{B22}$$

as shown in (33) and (34) in the main text. The leading-order solution is now complete.

Apart from building intuition for the local response, this analytical solution can now also be used to explicitly couple the local response to the barotropic circulation via the bottom stress curl. By nature of the large vertical shear in the bottom BL correction, it dominates the bottom stress at leading order:

$$\varepsilon^2\nu\frac{\partial \mathbf{u}}{\partial z}\bigg|_{-H} = \varepsilon^2\nu\frac{\partial \mathbf{u}_I}{\partial z}\bigg|_{-H} + \varepsilon\nu\frac{\partial \mathbf{u}_B}{\partial \overline{z}}\bigg|_0. \tag{B23}$$

The leading-order bottom stress is therefore of $O(\varepsilon)$ and, using $\mathbf{u}_{I0}|_{-H}$ from (B21) and (B22), takes the form

$$\varepsilon\nu\frac{\partial u_{B0}}{\partial \overline{z}}\bigg|_0 = \varepsilon\nu|_{-H}q_B\left[\frac{U_0 - V_0}{H} - \frac{1}{fH}\int_{-H}^0 z\left(\frac{\partial b}{\partial x} + \frac{\partial b}{\partial y}\right)dz - \frac{\tau^x + \tau^y}{fH}\right], \tag{B24}$$

$$\varepsilon\nu\frac{\partial v_{B0}}{\partial\bar{z}}\bigg|_0 = \varepsilon\nu|_{-H}q_B\left[\frac{U_0+V_0}{H}+\frac{1}{fH}\int_{-H}^{0}z\left(\frac{\partial b}{\partial x}-\frac{\partial b}{\partial y}\right)dz+\frac{\tau^x-\tau^y}{fH}\right], \tag{B25}$$

corresponding to (35) and (36) in the main text.

b. $O(\varepsilon)$ solution

In the main text, only the leading-order solution is presented. While this is sufficient for understanding the salient dynamics, it may be necessary to compute the $O(\varepsilon)$ contributions to obtain quantitative agreement with the numerical solution. This was the case for all cases in the main text, where the leading-order circulation set by thermal wind shear was weak. In appendix C, we will use this first-order solution to compute the $O(\varepsilon)$ contribution to Ψ, as shown in (42) and Fig. 8.

The interior equations [(B1) and (B2)] at $O(\varepsilon)$ are simply

$$\frac{\partial v_{I1}}{\partial z}=0 \quad\text{and}\quad \frac{\partial u_{I1}}{\partial z}=0, \tag{B26}$$

implying that u_{I1} and v_{I1} are constants in z. The bottom BL equations [(B6) and (B7)] are the same at $O(\varepsilon)$, implying the same form of the second-order BL correction $\mathbf{u}_{B1}$ as in (B9) and (B10), this time with the coefficients $\mathbf{u}_{I0}|_{-H}$ replaced by $\mathbf{u}_{I1}$. The integral will again pick up a factor of ε, yielding the $O(\varepsilon^2)$ contribution U_{B2} to the total transport. The surface boundary condition [(B14)] at $O(1)$ just becomes $\partial_{\hat{z}}\mathbf{u}_{S0}=0$ at $\hat{z}=0$, implying $\mathbf{u}_{S0}=0$, while at $O(\varepsilon)$, we have

$$\nu\frac{\partial u_{S1}}{\partial\hat{z}}=\frac{\nu}{f}\frac{\partial b}{\partial y} \quad\text{and}\quad \nu\frac{\partial v_{S1}}{\partial\hat{z}}=-\frac{\nu}{f}\frac{\partial b}{\partial x} \tag{B27}$$

at $\hat{z}=0$. If a buoyancy gradient at the surface exists, this will lead to an $O(\varepsilon)$ surface BL correction of the same form as in (B15) and (B16) with coefficients of the same form as in (B17) with $\boldsymbol{\tau}$ replaced by $-\nu\partial_z\mathbf{u}_{I0}|_0$. This correction yields an $O(\varepsilon^2)$ contribution to the vertically integrated transport $\mathbf{U}_{S2}$.

We again use the transport constraint to solve for $\mathbf{u}_{I1}$ in terms of $\mathbf{U}_1$. The $O(\varepsilon)$ transport is determined by the first-order barotropic interior correction and the integral of the leading-order bottom BL correction:

$$\mathbf{U}_1 = H\mathbf{u}_{I1}+\mathbf{U}_{B1}. \tag{B28}$$

Substituting the form of $\mathbf{U}_{B1}$ from (B11) and (B12) and solving for $\mathbf{u}_{I1}$ yields

$$u_{I1}=\frac{U_1}{H}+\frac{u_{I0}|_{-H}+v_{I0}|_{-H}}{2Hq_B}, \tag{B29}$$

$$v_{I1}=\frac{V_1}{H}-\frac{u_{I0}|_{-H}-v_{I0}|_{-H}}{2Hq_B}, \tag{B30}$$

where $\mathbf{u}_{I0}|_{-H}$ can be read off from (B21) and (B22). The $O(\varepsilon^2)$ bottom stress from (B23) is then

$$\varepsilon^2\nu\frac{\partial u_{I0}}{\partial z}\bigg|_{-H}+\varepsilon^2\nu\frac{\partial u_{B1}}{\partial\bar{z}}\bigg|_0=-\varepsilon^2\frac{\nu}{f}\frac{\partial b}{\partial y}\bigg|_{-H}+\varepsilon^2\nu|_{-H}q_B(u_{I1}-v_{I1}), \tag{B31}$$

$$\varepsilon^2\nu\frac{\partial v_{I0}}{\partial z}\bigg|_{-H}+\varepsilon^2\nu\frac{\partial v_{B1}}{\partial\bar{z}}\bigg|_0=+\varepsilon^2\frac{\nu}{f}\frac{\partial b}{\partial x}\bigg|_{-H}+\varepsilon^2\nu|_{-H}q_B(u_{I1}+v_{I1}). \tag{B32}$$

c. $O(\varepsilon^2)$ solution

Finally, we here present the results for the $O(\varepsilon^2)$ solution for completeness, which are not needed to understand the leading-order physics but are used to compute the solutions shown in Figs. 5 and 7 for quantitative comparison. The most important modification comes from the interior equations [(B1) and (B2)] at $O(\varepsilon^2)$,

$$-f\frac{\partial v_{I2}}{\partial z}=\frac{\partial^2}{\partial z^2}\left(\nu\frac{\partial u_{I0}}{\partial z}\right) \quad\text{and}\quad f\frac{\partial u_{I2}}{\partial z}=\frac{\partial^2}{\partial z^2}\left(\nu\frac{\partial v_{I0}}{\partial z}\right), \tag{B33}$$

or, after plugging in the leading-order solution [(B3)],

$$f^2\frac{\partial v_{I2}}{\partial z}=\frac{\partial^2}{\partial z^2}\left(\nu\frac{\partial b}{\partial y}\right) \quad\text{and}\quad f^2\frac{\partial u_{I2}}{\partial z}=\frac{\partial^2}{\partial z^2}\left(\nu\frac{\partial b}{\partial x}\right). \tag{B34}$$

The second-order correction to the flow can then be directly determined upon integration:

$$u_{I2}=u_{I2}|_{-H}+\frac{1}{f^2}\frac{\partial}{\partial z}\left(\nu\frac{\partial b}{\partial x}\right)-\frac{1}{f^2}\frac{\partial}{\partial z}\left(\nu\frac{\partial b}{\partial x}\right)\bigg|_{-H}, \tag{B35}$$

$$v_{I2}=v_{I2}|_{-H}+\frac{1}{f^2}\frac{\partial}{\partial z}\left(\nu\frac{\partial b}{\partial y}\right)-\frac{1}{f^2}\frac{\partial}{\partial z}\left(\nu\frac{\partial b}{\partial y}\right)\bigg|_{-H}, \tag{B36}$$

where again $u_{I2}|_{-H}$ and $v_{I2}|_{-H}$ are constants to be determined by the matching conditions. Integration over the column then yields a second-order contribution to the barotropic transport:

$$\int_{-H}^{0}u_{I2}\,dz=Hu_{I2}|_{-H}+\frac{\nu}{f^2}\frac{\partial b}{\partial x}\bigg|_0-\frac{\nu}{f^2}\frac{\partial b}{\partial x}\bigg|_{-H}-\frac{H}{f^2}\frac{\partial}{\partial z}\left(\nu\frac{\partial b}{\partial x}\right)\bigg|_{-H}\equiv U_{I2}, \tag{B37}$$

$$\int_{-H}^{0}v_{I2}\,dz=Hv_{I2}|_{-H}+\frac{\nu}{f^2}\frac{\partial b}{\partial y}\bigg|_0-\frac{\nu}{f^2}\frac{\partial b}{\partial y}\bigg|_{-H}-\frac{H}{f^2}\frac{\partial}{\partial z}\left(\nu\frac{\partial b}{\partial y}\right)\bigg|_{-H}\equiv V_{I2}. \tag{B38}$$

As at $O(\varepsilon)$, the $O(\varepsilon^2)$ bottom BL takes on the same form as (B9) and (B10), now with coefficients $u_{I2}|_{-H}$ and $v_{I2}|_{-H}$. This correction only modifies the transport by $O(\varepsilon^3)$. There is no surface BL correction at $O(\varepsilon^2)$ since the surface boundary condition [(B14)] at this order is simply $\partial_{\hat{z}}\mathbf{u}_{S2}=0$. As before, the coefficients for the second-order flow at the top of the bottom BL can be determined by writing the second-order transport in terms of its interior and BL contributions, $\mathbf{U}_2=\mathbf{U}_{I2}+\mathbf{U}_{B2}+\mathbf{U}_{S2}$, which becomes

$$U_2=Hu_{I2}|_{-H}-\frac{\nu}{f^2}\frac{\partial b}{\partial x}\bigg|_{-H}-\frac{H}{f^2}\frac{\partial}{\partial z}\left(\nu\frac{\partial b}{\partial x}\right)\bigg|_{-H}-\frac{u_{I1}+v_{I1}}{2q_B}, \tag{B39}$$

$$V_2 = Hv_{I2}|_{-H} - \frac{\nu}{f^2}\frac{\partial b}{\partial y}\bigg|_{-H} - \frac{H}{f^2}\frac{\partial}{\partial z}\left(\nu\frac{\partial b}{\partial y}\right)\bigg|_{-H} + \frac{u_{I1} - v_{I1}}{2q_B}, \tag{B40}$$

where u_{I1} and v_{I1} are determined above. Note that the surface terms in (B37) and (B38) cancel with those that appear from the surface BL correction U_{S2}.

d. Vertical flow

As described in the main text, the vertical flow can be determined from the horizontal flow by the frictional vorticity balance [(24)]. In general, this will require knowledge of how the horizontal flow varies in x and y due to the relative vorticity $\zeta = \partial_x v - \partial_y u$ term. For the special local responses shown in Fig. 5, however, a consistent local solution up to $O(\varepsilon)$ can be determined. The $O(1)$ and $O(\varepsilon)$ balances in the interior for (24) are

$$\beta v_{I0} = f\frac{\partial w_{I0}}{\partial z} \quad \text{and} \quad \beta v_{I1} = f\frac{\partial w_{I1}}{\partial z}. \tag{B41}$$

Using v_{I0} and v_{I1} from the previous sections, these can then be integrated from $z = 0$ to determine w_{I0} and w_{I1}. The constants of integration $w_{I0}|_0$ and $w_{I1}|_0$ are the zeroth- and first-order contributions to the Ekman pumping velocities, respectively. For the profiles in Fig. 5, these are zero. Due the ζ term in (24), computing the bottom BL correction will, in general, require evaluating gradients in the local solution across and along the slope. Instead, we make the simplifying assumption that, in the bottom BL, the flow is aligned with the slope:

$$w_{B0} = -H_x u_{B0} - H_y v_{B0} \quad \text{and} \quad w_{B1} = -H_x u_{B1} - H_y v_{B2}. \tag{B42}$$

In general, the matching conditions for w_0 and w_1 may not be satisfied with this assumption. For the simple cases of either along-slope symmetry or $U = V = 0$, however, the boundary condition holds.

APPENDIX C

Models for the Local Response to Mixing

The BL theory in appendix B is presented in terms of general expansions for the transports U and V and fully neglects the terms that arise when the aspect ratio is increased (appendix A). For the open-contour case, the local model simply sets $U = V = 0$, but the local model in the absence of along-slope variations instead assumes $U = 0$ and $\partial_z v|_{-H} = 0$. We here outline how one can solve for the expansions of V in the latter case and clarify how the BL theory can be modified to account for the added diffusion terms used in the numerical model. The models for the local response shown in Figs. 5 and 8 use these modifications.

a. Modification for $\alpha \neq 0$

Following appendix A, for $\partial_y b = 0$ and $H_y = 0$ (as is the case at $y = 0$ in the bowl), the frictional thermal wind equations [(21) and (22)] for an increased aspect ratio is approximately

$$-f\frac{\partial v}{\partial z} = -\frac{\partial b}{\partial x} + \Gamma^2\varepsilon^2\frac{\partial^2}{\partial z^2}\left(\nu\frac{\partial u}{\partial z}\right), \tag{C1}$$

$$f\frac{\partial u}{\partial z} = \Gamma\varepsilon^2\frac{\partial^2}{\partial z^2}\left(\nu\frac{\partial v}{\partial z}\right), \tag{C2}$$

where $\Gamma = 1 + \alpha^2 H_x^2$. This modification does not account for curvature in H. The BL theory for these equations follows the same procedure as in appendix B, now with $\partial_y b = 0$ and the added Γ terms. The most notable modification is in the BL equations, which become

$$-fv_B = \Gamma^2\nu|_{-H}\frac{\partial^2 u_B}{\partial\overline{z}^2}, \tag{C3}$$

$$fu_B = \Gamma\nu|_{-H}\frac{\partial^2 v_B}{\partial\overline{z}^2}, \tag{C4}$$

at the bottom and similarly for the surface. At $O(1)$, this leads to a modified bottom BL correction compared to (B9) and (B10) of the form

$$u_{B0} = -e^{-q_B\overline{z}}(u_{I0}|_{-H}\cos q_B\overline{z} + \Gamma^{-1/2}v_{I0}|_{-H}\sin q_B\overline{z}), \tag{C5}$$

$$v_{B0} = -e^{-q_B\overline{z}}(v_{I0}|_{-H}\cos q_B\overline{z} - \Gamma^{+1/2}u_{I0}|_{-H}\sin q_B\overline{z}), \tag{C6}$$

where now $q_B^{-1} = \Gamma^{3/4}\sqrt{2\nu|_{-H}/f}$. The BL solutions at other orders follow the same pattern. Thus, the added terms due to increasing the aspect ratio lead to a thicker BL by a factor of $\Gamma^{3/4}$ and a slightly asymmetrical Ekman spiral. The $O(1)$ and $O(\varepsilon)$ interior solutions are unchanged, but an extra factor of Γ does appear at $O(\varepsilon^2)$ compared to (B34):

$$f^2\frac{\partial u_{I2}}{\partial z} = \Gamma\frac{\partial^2}{\partial z^2}\left(\nu\frac{\partial b}{\partial x}\right). \tag{C7}$$

b. Assuming along-slope symmetry

We now turn specifically to the local model in the case of along-slope symmetry. From (B3), the leading-order interior cross-slope flow u_{I0} must be a constant since $\partial_y b = 0$. The transport constraint $U = 0$ then implies that this constant is zero so that $U_0 = Hu_{I0}|_{-H} = 0$. Setting the leading-order along-slope bottom stress from (B25) to zero implies that

$$V_0 = -\frac{1}{f}\int_{-H}^{0} z\frac{\partial b}{\partial x}\,dz, \tag{C8}$$

as in (42) in the main text. From (B5), this implies that $v_{I0}|_{-H} = 0$ as noted in PC23. Since the leading-order interior flow in both directions vanishes at the bottom, there is no leading-order BL correction: $\mathbf{u}_{B0} = 0$. Consequently, there is no $O(\varepsilon)$ contribution to the net transport from the cross-slope BL correction, and thus (B29) and (B30) imply that $u_{I1} = 0$ and $v_{I1} = V_1/H$. We can determine v_{I1} from setting the second-order along-slope bottom stress [(B32)] to zero, which yields

$$V_1 = -\frac{H}{fq_B}\frac{\partial b}{\partial x}\bigg|_{-H}, \tag{C9}$$

as in (42) in the main text. Note that q_B is modified for $\alpha \neq 0$ as described in the previous section. At the next order, we find that v_{I2} is a constant from (B36), and $U_2 = 0$ implies that

$$u_{I2}|_{-H} = \frac{\Gamma}{f^2}\frac{\partial}{\partial z}\left(\nu\frac{\partial b}{\partial x}\right)\bigg|_{-H}, \tag{C10}$$

from (B39), modified for the $\alpha \neq 0$ case. This yields

$$u_{I2} = \frac{\Gamma}{f^2}\frac{\partial}{\partial z}\left(\nu\frac{\partial b}{\partial x}\right), \tag{C11}$$

from (C7). As usual, these lead to an $O(\varepsilon^2)$ BL correction that contributes an $O(\varepsilon^3)$ term to the net transport. Setting the along-slope bottom stress from this correction to zero yields

$$v_{I2} = -u_{I2}|_{-H} = -\frac{\Gamma}{f^2}\frac{\partial}{\partial z}\left(\nu\frac{\partial b}{\partial x}\right)\bigg|_{-H}, \tag{C12}$$

so that

$$V_2 = -\frac{\Gamma H}{f^2}\frac{\partial}{\partial z}\left(\nu\frac{\partial b}{\partial x}\right)\bigg|_{-H} + \frac{1}{2fq_B^2}\frac{\partial b}{\partial x}\bigg|_{-H}, \tag{C13}$$

following (B40).

REFERENCES

Badia, S., and F. Verdugo, 2020: Gridap: An extensible finite element toolbox in Julia. *J. Open Source Software*, **5**, 2520, https://doi.org/10.21105/joss.02520.

Besard, T., C. Foket, and B. De Sutter, 2019: Effective extensible programming: Unleashing Julia on GPUs. *IEEE Trans. Parallel Distrib. Syst.*, **30**, 827–841, https://doi.org/10.1109/TPDS.2018.2872064.

Bezanson, J., A. Edelman, S. Karpinski, and V. B. Shah, 2017: Julia: A fresh approach to numerical computing. *SIAM Rev.*, **59**, 65–98, https://doi.org/10.1137/141000671.

Callies, J., 2018: Restratification of abyssal mixing layers by submesoscale baroclinic eddies. *J. Phys. Oceanogr.*, **48**, 1995–2010, https://doi.org/10.1175/JPO-D-18-0082.1.

——, and R. Ferrari, 2018: Dynamics of an abyssal circulation driven by bottom-intensified mixing on slopes. *J. Phys. Oceanogr.*, **48**, 1257–1282, https://doi.org/10.1175/JPO-D-17-0125.1.

Caulfield, C. P., 2021: Layering, instabilities, and mixing in turbulent stratified flows. *Annu. Rev. Fluid Mech.*, **53**, 113–145, https://doi.org/10.1146/annurev-fluid-042320-100458.

de Lavergne, C., G. Madec, J. L. Sommer, A. J. G. Nurser, and A. C. N. Garabato, 2016: On the consumption of Antarctic Bottom Water in the abyssal ocean. *J. Phys. Oceanogr.*, **46**, 635–661, https://doi.org/10.1175/JPO-D-14-0201.1.

Dell, R. W., and L. J. Pratt, 2015: Diffusive boundary layers over varying topography. *J. Fluid Mech.*, **769**, 635–653, https://doi.org/10.1017/jfm.2015.88.

Dewar, W. K., 1998: Topography and barotropic transport control by bottom friction. *J. Mar. Res.*, **56**, 295–328, https://doi.org/10.1357/002224098321822320.

Drake, H. F., R. Ferrari, and J. Callies, 2020: Abyssal circulation driven by near-boundary mixing: Water mass transformations and interior stratification. *J. Phys. Oceanogr.*, **50**, 2203–2226, https://doi.org/10.1175/JPO-D-19-0313.1.

Ekman, V. W., 1905: On the influence of the Earth's rotation on ocean currents. *Ark. Mat., Astron. Fys.*, **2**, 1–53.

Elman, H. C., D. J. Silvester, and A. J. Wathen, 2014: Finite elements and fast iterative solvers: with applications in incompressible fluid dynamics. *Numerical Mathematics and Scientific Computation*, 2nd ed. Oxford University Press, 1–479.

Ferrari, R., 2014: What goes down must come up. *Nature*, **513**, 179–180, https://doi.org/10.1038/513179a.

——, A. Mashayek, T. J. McDougall, M. Nikurashin, and J.-M. Campin, 2016: Turning ocean mixing upside down. *J. Phys. Oceanogr.*, **46**, 2239–2261, https://doi.org/10.1175/JPO-D-15-0244.1.

Garner, S. T., D. M. W. Frierson, I. M. Held, O. Pauluis, and G. K. Vallis, 2007: Resolving convection in a global hypohydrostatic model. *J. Atmos. Sci.*, **64**, 2061–2075, https://doi.org/10.1175/JAS3929.1.

Garrett, C., 1991: Marginal mixing theories. *Atmos.–Ocean*, **29**, 313–339, https://doi.org/10.1080/07055900.1991.9649407.

——, and E. Kunze, 2007: Internal tide generation in the deep ocean. *Annu. Rev. Fluid Mech.*, **39**, 57–87, https://doi.org/10.1146/annurev.fluid.39.050905.110227.

——, P. MacCready, and P. Rhines, 1993: Boundary mixing and arrested Ekman layers: Rotating stratified flow near a sloping boundary. *Annu. Rev. Fluid Mech.*, **25**, 291–323, https://doi.org/10.1146/annurev.fl.25.010193.001451.

Gent, P. R., and J. C. Mcwilliams, 1990: Isopycnal mixing in ocean circulation models. *J. Phys. Oceanogr.*, **20**, 150–155, https://doi.org/10.1175/1520-0485(1990)020<0150:IMIOCM>2.0.CO;2.

Geuzaine, C., and J.-F. Remacle, 2009: GMSH: A 3-D finite element mesh generator with built-in pre- and post-processing facilities. *Numer. Methods Eng.*, **79**, 1309–1331, https://doi.org/10.1002/nme.2579.

Guillén-González, F., and J. R. Rodríguez-Galván, 2015: Analysis of the hydrostatic Stokes problem and finite-element approximation in unstructured meshes. *Numer. Math.*, **130**, 225–256, https://doi.org/10.1007/s00211-014-0663-8.

Hallberg, R., and P. Rhines, 1996: Buoyancy-driven circulation in an ocean basin with isopycnals intersecting the sloping boundary. *J. Phys. Oceanogr.*, **26**, 913–940, https://doi.org/10.1175/1520-0485(1996)026<0913:BDCIAO>2.0.CO;2.

Holmes, R. M., C. D Lavergne, and T. J. McDougall, 2018: Ridges, seamounts, troughs, and bowls: Topographic control of the dianeutral circulation in the abyssal ocean. *J. Phys. Oceanogr.*, **48**, 861–882, https://doi.org/10.1175/JPO-D-17-0141.1.

Hughes, T. J. R., 1987: *The Finite Element Method: Linear Static and Dynamic Finite Element Analysis.* Prentice-Hall, 803 pp.

Ito, T., and J. Marshall, 2008: Control of lower-limb overturning circulation in the Southern Ocean by diapycnal mixing and mesoscale eddy transfer. *J. Phys. Oceanogr.*, **38**, 2832–2845, https://doi.org/10.1175/2008JPO3878.1.

Jansen, M. F., and L.-P. Nadeau, 2019: A toy model for the response of the residual overturning circulation to surface warming. *J. Phys. Oceanogr.*, **49**, 1249–1268, https://doi.org/10.1175/JPO-D-18-0187.1.

Kawase, M., 1993: Effects of a concave bottom geometry on the upwelling-driven circulation in an abyssal ocean basin. *J. Phys. Oceanogr.*, **23**, 400–405, https://doi.org/10.1175/1520-0485(1993)023<0400:EOACBG>2.0.CO;2.

Kuang, Z., P. N. Blossey, and C. S. Bretherton, 2005: A new approach for 3D cloud-resolving simulations of large-scale

atmospheric circulation. *Geophys. Res. Lett.*, **32**, L02809, https://doi.org/10.1029/2004GL021024.

Ledwell, J. R., E. T. Montgomery, K. L. Polzin, L. C. S. Laurent, R. W. Schmitt, and J. M. Toole, 2000: Evidence for enhanced mixing over rough topography in the abyssal ocean. *Nature*, **403**, 179–182, https://doi.org/10.1038/35003164.

Lumpkin, R., and K. Speer, 2007: Global Ocean meridional overturning. *J. Phys. Oceanogr.*, **37**, 2550–2562, https://doi.org/10.1175/JPO3130.1.

Luyten, J. R., J. Pedlosky, and H. Stommel, 1983: The ventilated thermocline. *J. Phys. Oceanogr.*, **13**, 292–309, https://doi.org/10.1175/1520-0485(1983)013<0292:TVT>2.0.CO;2.

MacCready, P., and P. B. Rhines, 1991: Buoyant inhibition of Ekman transport on a slope and its effect on stratified spin-up. *J. Fluid Mech.*, **223**, 631–661, https://doi.org/10.1017/S0022112091001581.

McDougall, T. J., 1989: Dianeutral advection. *Proc. Fifth 'Aha Huliko'a Hawaiian Winter Workshop on Parameterization of Small-Scale Processes*, Honolulu, HI, Hawaii Institute of Geophysics, 289–315, https://apps.dtic.mil/sti/tr/pdf/ADA213212.pdf#page=288.

——, and R. Ferrari, 2017: Abyssal upwelling and downwelling driven by near-boundary mixing. *J. Phys. Oceanogr.*, **47**, 261–283, https://doi.org/10.1175/JPO-D-16-0082.1.

Mertz, G., and D. G. Wright, 1992: Interpretations of the JEBAR term. *J. Phys. Oceanogr.*, **22**, 301–305, https://doi.org/10.1175/1520-0485(1992)022<0301:IOTJT>2.0.CO;2.

Montoison, A., and D. Orban, 2023: Krylov.jl: A Julia basket of hand-picked Krylovmethods. *J. Open Source Software*, **8**, 5187, https://doi.org/10.21105/joss.05187.

Munk, W., and C. Wunsch, 1998: Abyssal recipes II: Energetics of tidal and wind mixing. *Deep-Sea Res. I*, **45**, 1977–2010, https://doi.org/10.1016/S0967-0637(98)00070-3.

Munk, W. H., 1950: On the wind-driven ocean circulation. *J. Atmos. Sci.*, **7**, 80–93, https://doi.org/10.1175/1520-0469(1950)007%3C0080:OTWDOC%3E2.0.CO;2.

——, 1966: Abyssal recipes. *Deep-Sea Res. Oceanogr. Abstr.*, **13**, 707–730, https://doi.org/10.1016/0011-7471(66)90602-4.

Nikurashin, M., and R. Ferrari, 2011: Global energy conversion rate from geostrophic flows into internal lee waves in the deep ocean. *Geophys. Res. Lett.*, **38**, L08610, https://doi.org/10.1029/2011GL046576.

——, and G. Vallis, 2011: A theory of deep stratification and overturning circulation in the ocean. *J. Phys. Oceanogr.*, **41**, 485–502, https://doi.org/10.1175/2010JPO4529.1.

Pedlosky, J., 1965: A note on the western intensification of the oceanic circulation. *J. Mar. Res.*, **23**, 207–209, https://elischolar.library.yale.edu/journal_of_marine_research/1055.

——, 1979: *Geophysical Fluid Dynamics.* Springer, 624 pp.

Peterson, H. G., and J. Callies, 2022: Rapid spinup and spindown of flow along slopes. *J. Phys. Oceanogr.*, **52**, 579–596, https://doi.org/10.1175/JPO-D-21-0173.1.

——, and ——, 2023: Coupling between abyssal boundary layers and the interior ocean in the absence of along-slope variations. *J. Phys. Oceanogr.*, **53**, 307–322, https://doi.org/10.1175/JPO-D-22-0082.1.

Phillips, O. M., 1970: On flows induced by diffusion in a stably stratified fluid. *Deep-Sea Res. Oceanogr. Abstr.*, **17**, 435–440, https://doi.org/10.1016/0011-7471(70)90058-6.

——, J.-H. Shyu, and H. Salmun, 1986: An experiment on boundary mixing: Mean circulation and transport rates. *J. Fluid Mech.*, **173**, 473–499, https://doi.org/10.1017/S0022112086001234.

Polzin, K. L., J. M. Toole, J. R. Ledwell, and R. W. Schmitt, 1997: Spatial variability of turbulent mixing in the abyssal ocean. *Science*, **276**, 93–96, https://doi.org/10.1126/science.276.5309.93.

Rattray, M., 1982: A simple exact treatment of the baroclinicity-bathymetry interaction in a frictional, iterative, diagnostic ocean model. *J. Phys. Oceanogr.*, **12**, 997–1003, https://doi.org/10.1175/1520-0485(1982)012<0997:ASETOT>2.0.CO;2.

Rhines, P. B., 1975: Waves and turbulence on a beta-plane. *J. Fluid Mech.*, **69**, 417–443, https://doi.org/10.1017/S0022112075001504.

Robinson, A. R., 1970: Boundary layers in ocean circulation models. *Annu. Rev. Fluid Mech.*, **2**, 293–312, https://doi.org/10.1146/annurev.fl.02.010170.001453.

Ruan, X., and J. Callies, 2020: Mixing-driven mean flows and submesoscale eddies over mid-ocean ridge flanks and fracture zone canyons. *J. Phys. Oceanogr.*, **50**, 175–195, https://doi.org/10.1175/JPO-D-19-0174.1.

Salmon, R., 1998: *Lectures on Geophysical Fluid Dynamics.* Oxford University Press, 400 pp.

——, 2009: An ocean circulation model based on operator-splitting, Hamiltonian brackets, and the inclusion of sound waves. *J. Phys. Oceanogr.*, **39**, 1615–1633, https://doi.org/10.1175/2009JPO4134.1.

Sarkisyan, A. S., and V. F. Ivanov, 1971: Joint effect of baroclinicity and bottom relief as an important factor in the dynamics of sea currents. *Izv. Akad. Nauk SSSR, Fiz. Atmos. Okeana*, **7**, 173–188.

Schulman, E. E., 1975: A study of topographic effects. *Numerical Models of Ocean Circulation*, National Academy of Sciences, 147–165.

Smith, W. H. F., and D. T. Sandwell, 1997: Global sea floor topography from satellite altimetry and ship depth soundings. *Science*, **277**, 1956–1962, https://doi.org/10.1126/science.277.5334.1956.

Stommel, H., 1948: The westward intensification of wind-driven ocean currents. *Eos, Trans. Amer. Geophys. Union*, **29**, 202–206, https://doi.org/10.1029/TR029i002p00202.

Talley, L. D., 2013: Closure of the global overturning circulation through the Indian, Pacific, and Southern Oceans: Schematics and transports. *Oceanography*, **26** (1), 80–97, https://doi.org/10.5670/oceanog.2013.07.

Thompson, L., 1995: The effect of continental rises on the wind-driven ocean circulation. *J. Phys. Oceanogr.*, **25**, 1296–1316, https://doi.org/10.1175/1520-0485(1995)025<1296:TEOCRO>2.0.CO;2.

——, and G. C. Johnson, 1996: Abyssal currents generated by diffusion and geothermal heating over rises. *Deep-Sea Res. I*, **43**, 193–211, https://doi.org/10.1016/0967-0637(96)00095-7.

Thorpe, S. A., 1987: Current and temperature variability on the continental slope. *Philos. Trans. Roy. Soc.*, **A323**, 471–517, https://doi.org/10.1098/rsta.1987.0100.

Vallis, G. K., 2017: *Atmospheric and Oceanic Fluid Dynamics: Fundamentals and Large-Scale Circulation.* 2nd ed. Cambridge University Press, 946 pp.

Veronis, G., 1966: Wind-driven ocean circulation—Part 1. Linear theory and perturbation analysis. *Deep-Sea Res. Oceanogr. Abstr.*, **13**, 17–29, https://doi.org/10.1016/0011-7471(66)90003-9.

Waterhouse, A. F., and Coauthors, 2014: Global patterns of diapycnal mixing from measurements of the turbulent dissipation rate. *J. Phys. Oceanogr.*, **44**, 1854–1872, https://doi.org/10.1175/JPO-D-13-0104.1.

Welander, P., 1968: Wind-driven circulation in one- and two-layer oceans of variable depth. *Tellus*, **20** (1), 1–16, https://doi.org/10.1111/j.2153-3490.1968.tb00347.x.

Wenegrat, J. O., J. Callies, and L. N. Thomas, 2018: Submesoscale baroclinic instability in the bottom boundary layer. *J. Phys. Oceanogr.*, **48**, 2571–2592, https://doi.org/10.1175/JPO-D-17-0264.1.

Wolfe, C. L., and P. Cessi, 2011: The adiabatic pole-to-pole overturning circulation. *J. Phys. Oceanogr.*, **41**, 1795–1810, https://doi.org/10.1175/2011JPO4570.1.

Wunsch, C., 1970: On oceanic boundary mixing. *Deep-Sea Res. Oceanogr. Abstr.*, **17**, 293–301, https://doi.org/10.1016/0011-7471(70)90022-7.

Wynne-Cattanach, B. L., and Coauthors, 2024: Observations of diapycnal upwelling within a sloping submarine canyon. *Nature*, **630**, 884–890, https://doi.org/10.1038/s41586-024-07411-2.

Young, W. R., 2012: An exact thickness-weighted average formulation of the Boussinesq equations. *J. Phys. Oceanogr.*, **42**, 692–707, https://doi.org/10.1175/JPO-D-11-0102.1.